



Polytechnic Institute of Coimbra – Coimbra Health School

Radboud University Medical Centre – Nijmegen, The Netherlands

---

---

# **Implementation of an Enhanced Planar Processing Protocol in Clinical Practice**

Monique Inácio Gomes

**Masters in Nuclear Sciences Applied to Health**

**2014**



Polytechnic Institute of Coimbra – Coimbra Health School

Radboud University Medical Centre – Nijmegen, The Netherlands

---

---

## **Masters in Nuclear Sciences Applied to Health**

Masters' Dissertation

# **Implementation of an Enhanced Planar Processing Protocol in Clinical Practice**

Monique Inácio Gomes

**Supervisor:** Joana Margarida Rodrigues dos Santos

**Co-supervisor:** António Manuel Rodrigues Carvalho dos Santos

**Coimbra, October, 2014**

***This page intentionally left blank***

**“The mind that opens to a new idea never returns to its original size.”**

*Albert Einstein*

# Acknowledgments

Completing a thesis is definitely a challenge and I would not have been able to complete this journey without the invaluable support of many people and institutions. Therefore, I would like to thank all the people who contributed in some way to the work described in this dissertation, including those not mentioned here by name.

First, I would like to express my gratitude to my professor and the head of the Master Degree, Francisco Alves, for giving me the opportunity to do an internship, allowing me to open my mind to a new culture and to different ways of working and studying.

I cannot find enough words of thankfulness to Wim van den Broek, a superintendent technologist at Radboud University Medical Centre for his supervision, advice and guidance during my stay in Nijmegen, in The Netherlands.

The others Dutch mentors, Willem Grootjans and Eddy Mijnheere, also deserve a gratefully and sincerely thanks for their guidance, understanding, patience, and most importantly, their encouragement.

I would also like to thank all the support provided by the department's staff of Radboud University Medical Centre, who gave their help during the data collection and the data analysis throughout the whole internship.

My gratitude also goes to my Portuguese supervisors, Joana Santos and António Carvalho dos Santos, for their help, guidance and assistance.

Last, but certainly not the least, I would like to thank my family and my friends for their infinite love, support, tolerance and encouragement.

# Abstract

**Introduction:** Whole-body bone scan represents one of the most frequent diagnostic procedures in Nuclear Medicine. Such procedure requires an appropriated balance between image quality and radiation dose, which means collecting the minimum number of counts that provide an adequate image with diagnostic quality.

**Objective:** This study intends to apply the Enhanced Planar Processing (EPP) software, an image processing technique, in planar bone scintigraphic examinations of patients with metastatic disease from breast and prostate carcinomas. This aims to assess the performance of an EPP algorithm in clinical practice regarding diagnosis and reader confidence when the acquisition time is reduced in 50%.

**Material and Methods:** The present investigation was performed at the department of Radiology and Nuclear Medicine of Radboud University Nijmegen Medical Centre. Fifty one patients with suspected bone metastases were administered 500MBq 99m-technetium-labeled hydroxymethylene diphosphonate and scanned on a Siemens Symbia T16 or a Siemens Symbia S system. Each patient was imaged using standard clinical protocol (scan speed=8 cm/min) and with reduced acquisition time (scan speed=16 cm/min). Reduced scan time images were processed using Siemens EPP algorithm. All the images were submitted to an objective and subjective evaluation. Regarding the subjective assessment, three physicians evaluated the images concerning lesion detection, image quality, diagnostic acceptability, lesion location and diagnostic confidence. For the objective assessment, the selected regions for the Regions of Interest (ROIs) drawing were the third medium section of the femur and the soft tissue in the inner thigh in order to calculate the Signal-to-noise ratio (SNR), Contrast-to-noise ratio (CNR) and Coefficient of Variation (COV).

**Results:** The results show that the images processed with the EPP software provided the physicians with sufficient diagnostic information to detect metastases, since no significant differences were found ( $p>0.05$ ). Moreover, the interobserver agreement between these images and the images acquired with full-time protocol was 95% ( $k=0.88$ ). On the other hand, significant differences were found in terms of image quality comparing the three image types ( $p\leq 0.05$ ). Regarding to the diagnostic acceptability, no significant differences were found between full-count scans and EPP-Processed scans ( $p>0.05$ ), with an interobserver agreement of 70.6%. However, significant differences were found when physicians viewed the full-count scans and the half-count corresponding scans ( $p\leq 0.05$ ). In addition, no significant differences were found in terms of lesion location and diagnostic confidence ( $p>0.05$ ). Besides, no significant differences were found ( $p>0.05$ ) comparing the full-count and the EPP-Processes scans in terms of SNR, CNR and COV.

**Conclusion:** With this study results, it is possible to conclude that Siemens EPP algorithm offers a possibility to reduce the scan time in 50%, maintaining at the same time a diagnostically satisfying image quality. The utilization of this technology not only has the potential to increase patient satisfaction, but also helps the department's workflow.

## **Keywords**

- Bone scintigraphy
- Half-count scanning
- Enhanced planar processing
- Pixon algorithm

# Resumo

**Introdução:** A cintigrafia óssea é um dos exames mais frequentes em Medicina Nuclear. Esta modalidade de imagem médica requer um balanço apropriado entre a qualidade de imagem e a dose de radiação, ou seja, as imagens obtidas devem conter o número mínimo de contagem necessárias, para que apresentem qualidade considerada suficiente para fins diagnósticos.

**Objetivo:** Este estudo tem como principal objetivo, a aplicação do *software Enhanced Planar Processing* (EPP), nos exames de cintigrafia óssea em doentes com carcinoma da mama e próstata que apresentam metástases ósseas. Desta forma, pretende-se avaliar a *performance* do algoritmo EPP na prática clínica em termos de qualidade e confiança diagnóstica quando o tempo de aquisição é reduzido em 50%.

**Material e Métodos:** Esta investigação teve lugar no departamento de Radiologia e Medicina Nuclear do Radboud University Nijmegen Medical Centre. Cinquenta e um doentes com suspeita de metástases ósseas foram administrados com 500MBq de metilenodifosfonato marcado com tecnécio-99m. Cada doente foi submetido a duas aquisições de imagem, sendo que na primeira foi seguido o protocolo *standard* do departamento (*scan speed*=8 cm/min) e na segunda, o tempo de aquisição foi reduzido para metade (*scan speed*=16 cm/min). As imagens adquiridas com o segundo protocolo foram processadas com o algoritmo EPP. Todas as imagens foram submetidas a uma avaliação objetiva e subjetiva. Relativamente à análise subjetiva, três médicos especialistas em Medicina Nuclear avaliaram as imagens em termos da detetabilidade das lesões, qualidade de imagem, aceitabilidade diagnóstica, localização das lesões e confiança diagnóstica. No que respeita à avaliação objetiva, foram selecionadas duas regiões de interesse, uma localizada no terço médio do fémur e outra localizada nos tecidos moles adjacentes, de modo a obter os valores de relação sinal-ruído, relação contraste-ruído e coeficiente de variação.

**Resultados:** Os resultados obtidos evidenciam que as imagens processadas com o *software* EPP oferecem aos médicos suficiente informação diagnóstica na deteção de metástases, uma vez que não foram encontradas diferenças estatisticamente significativas ( $p > 0.05$ ). Para além disso, a concordância entre os observadores, comparando essas imagens e as imagens adquiridas com o protocolo *standard* foi de 95% ( $k=0.88$ ). Por outro lado, no que respeita à qualidade de imagem, foram encontradas diferenças estatisticamente significativas quando se compararam as modalidades de imagem entre si ( $p \leq 0.05$ ). Relativamente à aceitabilidade diagnóstica, não foram encontradas diferenças estatisticamente significativas entre as imagens adquiridas com o protocolo *standard* e as imagens processadas com o EPP *software* ( $p > 0.05$ ), verificando-se uma concordância entre os observadores de 70.6%. Todavia, foram encontradas diferenças estatisticamente significativas entre as imagens adquiridas com o



protocolo *standard* e as imagens adquiridas com o segundo protocolo e não processadas com o *software* EPP ( $p \leq 0.05$ ). Para além disso, não foram encontradas diferenças estatisticamente significativas ( $p > 0.05$ ) em termos de relação sinal-ruído, relação contraste-ruído e coeficiente de variação entre as imagens adquiridas com o protocolo *standard* e as imagens processadas com o EPP.

**Conclusão:** Com os resultados obtidos através deste estudo, é possível concluir que o algoritmo EPP, desenvolvido pela *Siemens*, oferece a possibilidade de reduzir o tempo de aquisição em 50%, mantendo ao mesmo tempo uma qualidade de imagem considerada suficiente para fins de diagnóstico. A utilização desta tecnologia, para além de aumentar a satisfação por parte dos doentes, é bastante vantajosa no que respeita ao *workflow* do departamento.

## Palavras-chave

- Cintigrafia Óssea
- Half-count scanning
- Enhanced planar processing
- Algoritmo Pixon

# Contents

List of Abbreviations.....	x
Index of Figures.....	xi
Index of Tables.....	xii
Index of Equations.....	xiii
Introduction.....	1
Metastatic Bone Disease and Nuclear Medicine Imaging.....	2
1. Metastatic bone disease.....	3
1.1. Pathophysiology of Bone Metastases.....	3
1.2. Clinical Presentation.....	5
1.2.1. Pain.....	5
1.2.2. Pathological Fracture.....	5
1.2.3. Hypercalcemia.....	6
1.2.4. Spinal instability with cord compression.....	6
1.3. Imaging Diagnosis.....	6
1.3.1. Radiography.....	8
1.3.2. <sup>99m</sup> Tc-Bone Scan.....	8
1.3.3. Computed Tomography and Magnetic Resonance Imaging.....	9
1.3.4. PET-CT.....	9
2. Planar Nuclear Imaging.....	11
2.1. Gamma Camera.....	11
2.1.1. Physics and Instrumentation.....	12
2.1.1.1. Collimator.....	12
2.1.1.2. Scintillation Crystal.....	14
2.1.1.3. Photomultiplier Tubes.....	16
2.1.1.4. Associated Electronics.....	17
2.2. Measures of Performance.....	18
2.2.1. Resolution.....	18
2.2.2. Sensitivity.....	18
2.2.3. Uniformity.....	18
2.2.4. Dead Time.....	19
2.3. Bone Scintigraphy.....	19
2.3.1. Radiopharmaceutical – <sup>99m</sup> Tc.....	19

2.3.1.1.	Mechanism of Accumulation.....	20
2.3.1.2.	Patient Preparation.....	21
2.3.1.3.	Imaging Metastatic Disease .....	21
2.3.1.4.	Imaging Technique .....	22
2.4.	Pitfalls and Artefacts.....	23
3.	Reducing Scan Time in Bone Scintigraphy .....	24
4.	Processing Scintigraphic Images .....	26
4.1.	Image Quality in Nuclear Medicine .....	26
4.1.1.	Spatial Resolution.....	27
4.1.2.	Point Spread Function .....	27
4.1.3.	Signal-to-Noise Ratio.....	28
4.1.4.	Contrast.....	28
4.1.5.	Noise.....	29
4.2.	Image Reconstruction.....	30
5.	Pixon Method.....	31
	Enhanced Planar Processing in Clinical Practice.....	38
6.	Purpose of the Study.....	39
7.	Materials and Methods.....	40
7.1.	Patient Population and Image Acquisition .....	41
7.2.	Organizing the Collected Data .....	42
7.3.	Image Assessment.....	42
7.3.1.	Subjective Analysis .....	43
7.3.2.	Objective Analysis.....	45
7.4.	Statistical Analysis .....	46
8.	Results.....	47
8.1.	Sample Characterization .....	47
8.2.	Subjective Assessment .....	47
8.2.1.	Metastatic Lesion Detection .....	47
8.2.2.	Image Quality.....	48
8.2.3.	Diagnostic Acceptability.....	49
8.2.4.	Anatomical Location .....	52
8.2.5.	Diagnostic Confidence.....	53
8.3.	Objective Assessment.....	55
8.3.1.	SNR, CNR and COV .....	55

9.	Discussion.....	56
9.1.	Subjective Assessment.....	56
9.1.1.	Metastatic Lesion Detection.....	57
9.1.2.	Image Quality.....	57
9.1.3.	Diagnostic Acceptability .....	58
9.1.4.	Lesion Location .....	58
9.1.5.	Diagnostic Confidence .....	59
9.2.	Objective Assessment .....	59
9.2.1.	SNR, CNR and COV .....	59
9.3.	Limitations .....	60
10.	Conclusion.....	61
	Bibliographic References.....	62
	Appendix I.....	67
	Appendix II.....	69
	Appendix III.....	70
	Appendix IV .....	73
	Appendix V .....	74
	Appendix VI .....	75
	Appendix VII .....	76

## List of Abbreviations

CNR	Contrast-to-noise Ratio
COV	Coefficient of Variation
CT	Computed Tomography
EANM	European Association of nuclear Medicine
EPP	Enhanced Planar Processing
18-FDG	Fluorodeoxyglucose
FPB	Fractal Pixon Basis
FWHM	Full Width at Half Maximum
LEHR	Low Energy High Resolution
MRI	Magnetic Resonance Imaging
NaI(Tl)	Thallium Activated Sodium Iodide
PET	Positron Emission Tomography
PMT	Photomultiplier Tubes
PSF	Point Spread Function
ROI	Region of Interest
ROIs	Regions of Interest
SNR	Signal-to-noise Ratio
SPECT	Single-photon Emission Computed Tomography
SPSS	Statistical Package for the Social Sciences
SS	Skeletal Scintigraphy
Tc	Technetium
UPB	Uniform Pixon Basis

## Index of Figures

<b>Figure 1</b> - Mechanism of tumour metastasis to bone .....	4
<b>Figure 2</b> - Suggested algorithm of imaging studies for the osseous metastases .....	7
<b>Figure 3</b> - Schematic bone structure and types of metastasis observed by imaging modalities.....	7
<b>Figure 4</b> - Diagram representing the components inside a gamma camera.....	11
<b>Figure 5</b> - Schematic of a gamma camera .....	12
<b>Figure 6</b> - Diverging and converging gamma camera collimators.....	13
<b>Figure 7</b> - Main collimator configurations and their effect on the acquired image .....	14
<b>Figure 8</b> - Schematic cross-section of a NaI(Tl) crystal for a gamma camera .....	15
<b>Figure 9</b> - Basic structure of a photomultiplier tube.....	16
<b>Figure 10</b> - Diagram of a scintillation detector.....	17
<b>Figure 11</b> - Gamma ray production .....	20
<b>Figure 12</b> - Subdivision of the gamma camera detector area for generating a digital image .....	24
<b>Figure 13</b> - Radiation profile and Relative FWHM for parallel-hole collimator .....	27
<b>Figure 14</b> - Pixon reconstruction of a satellite survey scan.....	31
<b>Figure 15</b> - Pixon reconstruction of a digital Nuclear Medicine planar image.....	32
<b>Figure 16</b> - Performance of the Pixon method for the “Lena” Matlab image .....	33
<b>Figure 17</b> - Example of a Pixon image model and its correspondent graph structure.....	33
<b>Figure 18</b> - Pseudo image and its correspondent Pixon map.....	34
<b>Figure 19</b> - Pixon image reconstruction for a synthetic data set .....	35
<b>Figure 20</b> - Block diagram of the steps of image reconstruction with Pixon map calculation .....	36
<b>Figure 21</b> - Simulated image reconstruction sequence.....	37
<b>Figure 22</b> - Scheme of the Methodology used in this study .....	40
<b>Figure 23</b> - Reconstruction parameters applied in the EPP software .....	42
<b>Figure 24</b> - First question of the assessment form about metastatic lesion detection .....	43
<b>Figure 25</b> - Second and third questions of the assessment form.....	44
<b>Figure 26</b> - Human skeleton diagram of the assessment form .....	44
<b>Figure 27</b> - The two circular ROIs set in the images.....	45
<b>Figure 28</b> - Combined image quality scores of the three observers by image type .....	49
<b>Figure 29</b> - Combined diagnostic acceptability scores of the three observers by image type .....	51
<b>Figure 30</b> - Frequency of bone metastases in patients with prostate and breast cancer.....	52

**Index of Tables**

**Table 1** – Incidence of bone metastases in different types of cancer.....3

**Table 2** – Number of scans diagnosed with metastatic bone disease ..... 47

**Table 3** – Number of cases scored according to the scoring form for the image quality ..... 48

**Table 4** - Number of cases scored according to the scoring form for the diagnostic acceptability..... 50

**Table 5** – Interobserver agreement rates ..... 53

**Table 6** – Confidence of physicians in deciding whether an image represents metastatic disease. .... 54

**Table 7** – Mean ± standard deviation of SNR, CNR and COV for each image type. .... 55

**Index of Equations**

**Equation 1** – Signal-to-noise Ratio ..... 28

**Equation 2** – Acquired Image ..... 29

**Equation 3** – Image Reconstruction ..... 30

**Equation 4** - Image as an integral over a pseudo image ..... 35

**Equation 5** – Signal-to-noise Ratio (Methodology)..... 46

**Equation 6** – Contrast-to-noise Ratio (Methodology)..... 46

**Equation 7** – Coefficient of Variation (Methodology)..... 46



## **Introduction**

In advanced oncologic conditions, the development of metastatic bone disease can be a common and severe complication. This condition is of particular interest in high prevalence carcinomas such as those in the breast and prostate, where bone is a common site for metastases.

Metastatic bone lesions put patients at high risk of skeletal complications, being also related to increased morbidity and decreased survival. Bone involvement in its clinical presentation may include pain and pathological fracture, contributing to a decreased in the quality of life.

There are several kinds of imaging available for the study of bone metastases. Each imaging technique depicts different aspects of tissues, influencing the appearance of the different malignant bone lesions. Thus, due to its great overall sensitivity, whole-body planar bone scintigraphy has been considered as the standard technique for bone metastases screening. This imaging technique provides the essential information concerning location, prognosis and evaluation of response to therapy.

Since pain is the most common presented symptom, patient care should never be forgotten. Diagnostic imaging procedures are not an exception. Thus, the professionals must look for the best techniques and methods that are suitable for each patient so the procedures can be successfully performed with minimal discomfort to the patient.

In the particular case of bone scintigraphy, patient care can be improved by means of reducing the acquisition time. This practice needs an appropriate balance between the time and the image quality. To obtain an accurate clinical diagnosis, further image processing techniques may be implemented. However, the best method for noise reduction must be found in order to sustain diagnostic confidence.

# **Metastatic Bone Disease and Nuclear Medicine Imaging**

## 1. Metastatic bone disease

In advanced oncologic disease, the development of metastatic bone disease can be a common and severe complication (**Table 1**). Bone is the most common site for metastasis in cancer and is of particular interest in breast and prostate cancers because of the prevalence of these diseases. Up to 70% of patients with these cancers develop this condition. The sternum is a common site for solitary skeletal metastasis in breast cancer, while the spine is the most common site of metastases in prostate carcinoma. Carcinomas of lung, kidney, thyroid and melanomas are other common tumours that metastasize to bone (1-5).

Bone lesions put these patients at high risk of skeletal complications. It is a condition associated with increased morbidity and reduced survival. The major complications related to bone involvement are severe and debilitating pain, spinal cord compression and pathological fracture, which contribute to the decreased quality of life of the patient (1,2,6).

**Table 1** – Incidence of bone metastases in different types of cancer and the median survival (**6**).

CANCER	FIVE-YEAR WORLD PREVALENCE <sup>1</sup>	INCIDENCE OF BONE METASTASES IN CANCERS <sup>2</sup>	MEDIAN SURVIVAL (MONTHS) <sup>2,3</sup>
Myeloma	144,000	70%–95%	6–54
Renal	480,000	20%–25%	6
Melanoma	533,000	14%–45%	6
Thyroid	475,000	60%	48
Lung	1,394,000	30%–40%	6
Breast	3,860,000	65%–75%	19–25
Prostate	1,555,000	65%–75%	12–53

### 1.1. Pathophysiology of Bone Metastases

Normal bone undergoes continuous remodelling. It is a lifelong process essential to maintain mechanical function wherein old bone is removed from the skeleton through resorption and new bone is added by ossification. Bone remodelling involves continuous removal of discrete packets of old bone, replacement of these packets with newly synthesized proteinaceous matrix and subsequent mineralization of the matrix to form new bone. Thus, bone is added where needed and removed where it is not required. This process is necessary to maintain the structural integrity of the skeleton as well as to support its metabolic functions as a storehouse of calcium and phosphorus (1,7).

The mechanisms of bone formation and bone removal represent two tightly coordinated events of the normal remodelling cycle. They require synchronized activities of multiple cellular participants to ensure their sequentially occurrence at the same anatomical location in order to preserve bone mass. Consequently, this process depends on the orderly development and activation of osteoclasts and osteoblasts, involving series of highly regulated stages that depend on the interactions of these two cell line ages (6). In many advanced cancers, the skeleton, after the lungs and liver, is the third most common site of metastatic disease. The metastasis of tumour cells to the bone matrix involves a complex cascade of events (**Figure 1**) (6,8).

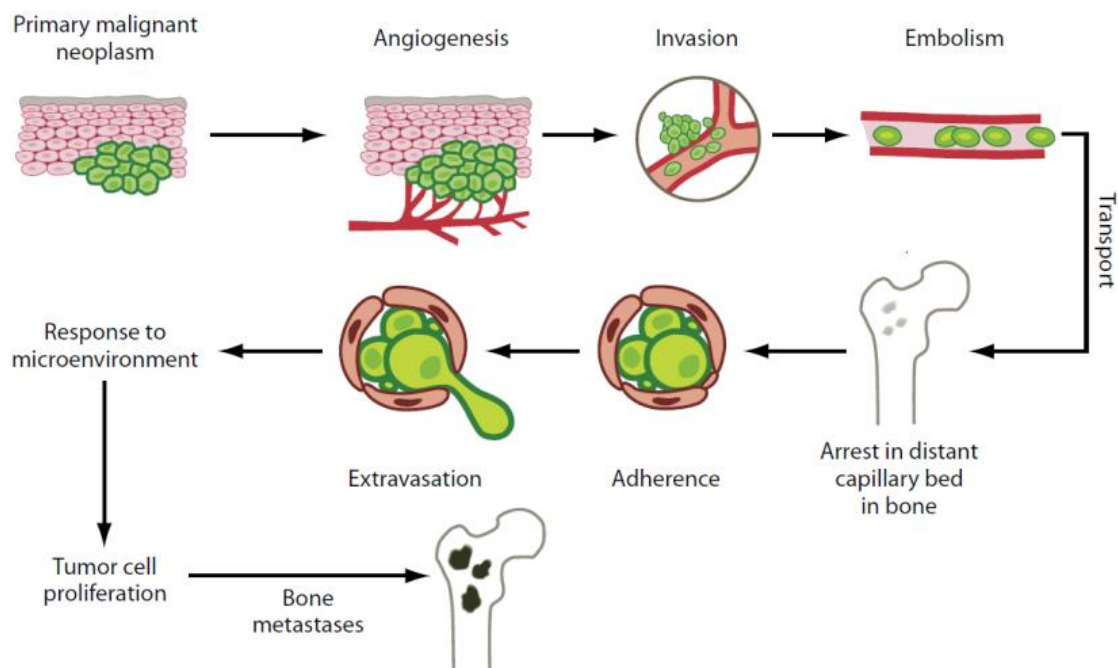


**Figure 1** - Mechanism of tumour metastasis to bone (7).

This multistep mechanism involves a bidirectional interaction of the tumour cells with cellular elements in three different microenvironments: the site of primary malignant neoplasm, the transport and the bone microenvironment (2).

Bone metastasis begins when primary tumour cells detach from their place of origin (primary tumour) by forming new blood vessels (angiogenesis), invading the vasculature. Thus, they will reach the skeletal sites by adhering the vascular endothelial cells of distant capillaries of the bone. When the cells escape the circulation they can establish themselves, proliferate and then induce metastatic lesions. Once tumour cells have colonized the bone matrix, they secrete a large number of soluble growth factors that stimulate the activity of osteoclasts and/or osteoblasts, disrupting normal bone remodelling (2,6).

## **1.2. Clinical Presentation**

Metastatic bone disease is the cause of considerable morbidity in advanced cancer situations. The clinical presentation of this condition includes pain, pathological fracture, hypercalcemia and spinal instability with medullar compression (4,5).

### **1.2.1. Pain**

The clinical presentation of metastatic bone disease is variable, but pain is the most common presenting symptom with either osteolytic or osteoblastic lesions. This condition is shown in 75% of patients during this type of clinical evaluation. Painless lesions are usually diagnosed during staging follow-up examinations to patients with a known history of carcinoma. Pain incompletely relieved by rest and night pain are not specific indications of metastasis, however they are typical symptoms. Furthermore, weightbearing bones may become symptomatic early in the course of disease, whereas bones such as the flat bones of ribs or sternum may remain asymptomatic until late in the disease, often until pathologic fracture occurs (8).

Different sites of bone metastases are related with distinct pain syndromes. Common sites of metastatic involvement associated with pain are the base of skull, vertebrae, pelvis and femur (3).

Lytic lesions with bone loss are usually associated with mechanical pain, whilst blastic lesions can cause functional pain through the loss of bone's structural integrity. The tumour type, location, number or size of metastases and the patient's characteristics are not correlated with the presence of and the severity of pain. In general, this complaint develops gradually becoming progressively more severe. It can be divided into two types of pain according to the presented symptoms (continuous or incident pain) and the mechanism of the disease (primary or secondary). Primary pain involves bone resorption with disruption of skeletal architecture and microfracture. In contrast, secondary pain is characterized by nerve root infiltration or compression and reactive muscle spasm. For this reason, effective treatments are needed in order to improve the patient's quality of life (1).

### **1.2.2. Pathological Fracture**

The term pathological fracture refers to the fracture that occurs in the area of a neoplasm. It can be caused by any type of bone tumour, but the majority are secondary to metastatic carcinomas. In some conditions, it might be the first sign of bone metastasis. Despite the fact that the incidence is uncertain, breast cancer is the most common primary site. The destruction of cortical bone by the tumour cells will result in trabecular disruption and

microfractures with consequent total loss of bone integrity. This type of fracture can occur spontaneously or after a minor injury, but its probability increases with the duration of the metastatic involvement (4,7).

### **1.2.3. Hypercalcemia**

Hypercalcemia is defined as an elevation of plasmatic ionized calcium. In most cases, hypercalcemia is a result of bone destruction, and osteolytic metastases are observed in 80% of cases. This clinical feature occurs particularly in patients with breast malignancies, reflecting an association with the presence of liver metastases. The signs and symptoms of hypercalcemia are nonspecific, but normally include pain, fatigue, anorexia and constipation. If untreated, the result will be the deterioration of renal function and mental status (4,5).

### **1.2.4. Spinal instability with cord compression**

Spine is the most common site of bone metastasis, making neurologic symptoms and spinal instability very frequent. Spinal instability will lead to mechanical pain with consequent impact on quality of life. Besides, spinal cord compression is referred as a medical emergency, which requires urgent evaluation and treatment. Local pain usually precedes radicular pain and may predate the appearance of other neurologic signs by weeks or months (4,5).

## **1.3. Imaging Diagnosis**

There are several imaging modalities available for the study of bone metastases. To increase the probability of detecting bone metastases in a timely and cost-effective manner, the most effective imaging procedures must be requested (**Figure 2**) (9).

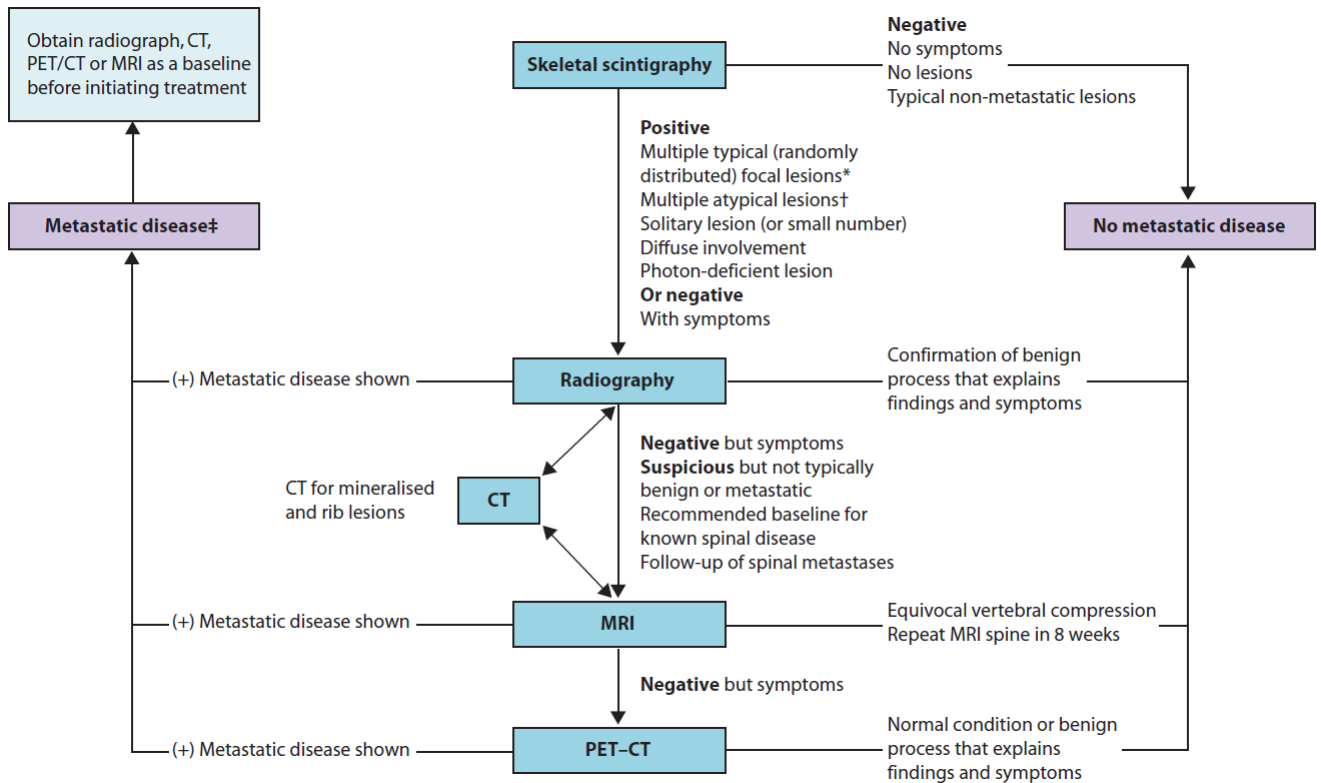


**Figure 2** - Suggested algorithm of imaging studies for the osseous metastases (9).

Each imaging modality depicts different aspects of tissues. Hence, the appearance of the various types of bone lesions can considerably differ depending on the imaging technique (Figure 3) (10).

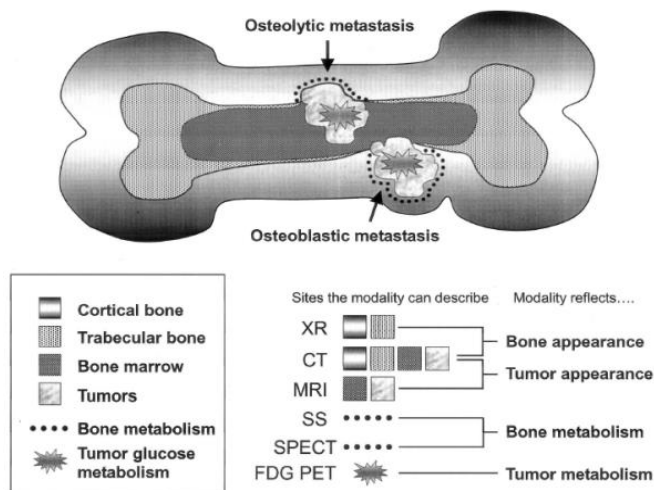


**Figure 3** - Schematic bone structure and types of metastasis observed by a wide range of imaging modalities: Plain Radiograph (XR), Computed Tomography (CT), Magnetic Resonance Imaging (MRI), Skeletal Scintigraphy (SS), Single Photon Emission Computed Tomography (SPECT) and Positron Emission Tomography (18-FDG-PET) (10).

### **1.3.1. Radiography**

For some types of tumor, skeletal metastases are readily detected by radiological studies, forming an important aspect of clinical disease management. Thus, the radiological evaluation of focal symptoms is the first step in the assessment of suspected bone metastases, to visualize the painful area and assess the structural integrity of the bone. However, it is not generally recommended as a screening method due to its poor sensitivity, which depends partly on lesion location (6,8,10).

Apart from the limited contrast for differentiation of the various soft tissues, the main disadvantage of this method is that anatomical structures are projected in one plan, leading to superimposition of a metastatic nodule with normal anatomic structures. Still, radiography may help to distinguish metastases from another conditions along with accessing the risk of pathological fracture (11).

Bone metastases are classified regarding the radiological classification of the observed changes in bone architecture, being usually described as: osteolytic, when bone destruction arises by the action of osteoclasts, as observed in breast cancer patients; osteoblastic, which are characterized by sclerosis, being predominant in prostate cancer conditions; or mixed, where both processes of resorption and formation occur at the same time. Although, it is important to remember that any cancer can appear in any pattern (3,4,6).

Radiographs are important for the interpretation of abnormal findings in the 99m-technetium bone scan, which should be correlated prior to confirming the diagnosis of metastatic bone disease (8).

### **1.3.2. 99m-Technetium Bone Scan**

Since the introduction of 99m-technetium-based scan agents, the radioisotope bone scan has been the standard method for detection of skeletal metastases. This imaging method is more sensitive than radiography for detection of other skeletal sites of tumour involvement. Despite its low specificity and higher false-positive rates, it can detect these lesions earlier than plain films. False-negative findings can appear when pure osteolytic metastases are growing rapidly, when bone turnover is slow or when the site is avascular (7,9,10).

Skeletal scintigraphy (SS) is generally considered sensitive for detecting osteolytic or osteoblastic bone metastases on whole-body images. Moreover, the advantage of this kind of examination is not for diagnosis but rather for screening, as it is widely available and can produce quick images at reasonable cost (10).

Due to its particular interest for this study, this topic will be further discussed on the next chapter.



### **1.3.3. Computed Tomography and Magnetic Resonance Imaging**

Computed Tomography (CT) and Magnetic Resonance Imaging (MRI) can depict anatomic changes in more detail than SS (9).

CT is the study of choice when looking for bone detail and cortical damage since delineates cortex and can help the description of abnormal calcifications. Due to its technical advantages, CT is the most frequently used imaging diagnostic method for diagnosis, staging and detection of nodal and distant metastases, monitoring and follow-up in oncology (7,8,11).

For accessing bone metastases, MRI is preferable to CT due to its excellent soft-tissue contrast resolution, which allows better depiction of the marrow cavity and adjacent soft-tissues. MRI is often performed at the site of metastatic disease, being useful in cases in which the bone scan is negative but localized symptoms are present. This imaging technique is very sensitive to early marrow replacement and can locate metastases prior to their appearance on radiographs and CT scans, even with low resolution for bony anatomy. Through this study is also possible to distinguish between osteoporotic and malignant fractures (4,7,10).

If MRI and CT are not capable of detecting the disease and clinical suspicion of bone metastasis remains, the use of PET-CT is recommended (9).

### **1.3.4. PET-CT**

Positron Emission Tomography (PET) is a tomographic technique that produces high-resolution images with three-dimensional distribution of radioactivity through the detection of high-energy photon pairs, emitted by the positron emitter labelled radioisotope. The glucose analogue 18-fluorodeoxyglucose (18-FDG) is the most commonly used tracer since the accumulation in tissue is proportional to the amount of glucose utilization. This radiopharmaceutical is wide used in oncology because of the high glucose uptake by many tumours (7,11).

In opposition to PET, CT generates tomographic images using an x-ray source. This imaging technique produces morphological and anatomic views with high resolution. Therefore, the information derived from CT can be used to increase the precision of localization, extent and characterization of lesions detected by 18-FDG PET (12).

The combination of PET and CT has recently revealed various implications for evaluating bone metastases. Due to its high sensitivity, fluorine 18-FDG PET is the modality of choice for standard oncologic staging, restaging and treatment monitoring evaluations. Besides, CT data of the PET-CT studies allows the reduction of false-positive rate by determining the

morphology of the scintigraphic lesions through fusion of functional images with the anatomic dataset (7,12,13).

PET-CT allows soft-tissue contrast resolution that is absent with bone scintigraphy. Thus, it can help better differentiate whether FDG-avid lesions are truly located within bone versus adjacent soft tissue (13).

## 2. Planar Nuclear Imaging

Nuclear Medicine is a diagnostic imaging modality in which information is obtained from the way the tissues and organs process radiolabeled compounds. The main purpose is the quantitative measurement of physiologic and biochemical characteristics of the body. This involves administering a radioactive agent, which will be carried throughout the body by circulation and then taken up by organs where radioactive decay within the patient begins. This means that the unstable nuclei will decay to a more stable state by emitting energy in the form of radiation such as gamma rays. Radioactive decay has applications in medicine for both diagnostic and therapeutic purposes (14-16).

The emitted radiation has high energy and can be detected and measured by suitable detection devices. The majority of those radiotracers used in diagnostic imaging are gamma emitters. That type of radiation can be detected by using imaging devices such as gamma scintillation cameras, Single-Photon Emission Computed Tomography (SPECT) and PET scanners. In the particular case of planar scintigraphy, a simple gamma scintillation camera should be used (14,17).

### 2.1. Gamma Camera

There are two types of nuclear imaging methods: single-photon imaging and PET. These two methods are distinguished by the physical properties of the administered radioisotopes, which can radioactively decay by single or double-photon emission (14).

A gamma camera is a single-photon imaging technique, also referred to as a scintillation camera or Anger camera, being the primary imaging instrument used in Nuclear Medicine. The basic components of a gamma camera system are the collimator, the scintillation (or semiconductor) detector and readout electronics (**Figure 4**) (15-17).

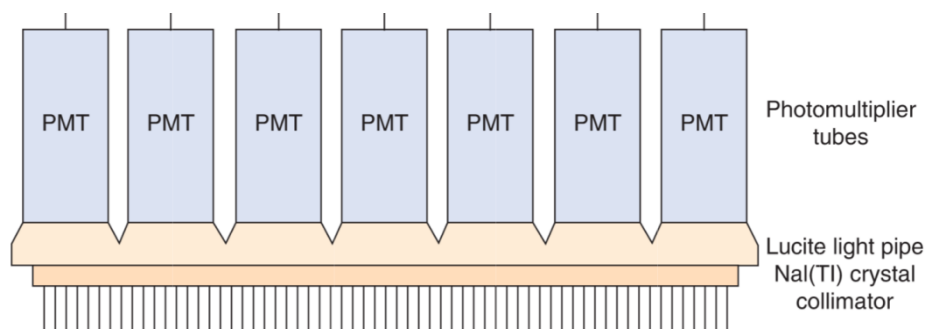


**Figure 4** - Diagram representing the components inside a gamma camera (15).

Gamma cameras are used in both planar imaging and SPECT. Planar imaging produces a two-dimensional image of a three-dimensional object. Those images contain no depth information and some structures can be superimposed. To overcome this drawback, at least two views of the patient should be taken, depending on the procedure. For transaxial tomography (SPECT), the camera is rotated around the patient, acquiring multiple views from different angles. These projections are used to calculate the transverse activity distribution, applying suitable reconstruction methods. This procedure is performed with either rotating Anger cameras (with two or three camera heads) or specific ring or partial ring detector systems (18-20).

### 2.1.1. Physics and Instrumentation

The principle of gamma cameras relies on the conversion of the photons emitted by the radionuclide in the patient into a light pulse and subsequently into a voltage signal (**Figure 5**). This signal is used to create an image which reflects the distribution of the radionuclide. Thus, scintigraphic instrumentation consists of scintillation crystals to convert gamma ray energy (photons) into visible light, specific light sensors, readout electronics and image processing units (17,18,19,21).

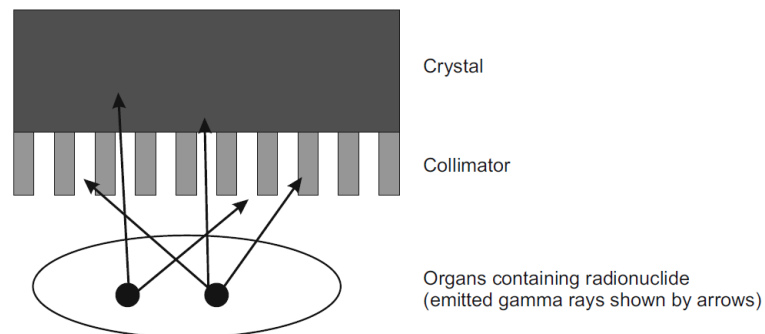


**Figure 5 - Schematic of a gamma camera (16).**

#### 2.1.1.1. Collimator

The collimator is a device placed between the crystal and the object of study with the main function of limiting the photons that interact with the crystal to only those that have a specific path relative to the detector surface. Despite the fact that collimators make the systems less efficient by reducing the counting rate, they are essential for the formation of the image since the emission of gamma rays from the patient is isotropic (19,22).

Lead is usually the material of choice for collimators due to the combination of high density with high atomic number. High density materials are required due to the correlation between the attenuation coefficient, which must be high to ensure gamma photon absorption (17).

There are two basic types of collimators which can be defined as multihole and pinhole:

A multihole collimator consists of a gamma radiation absorbing material with great abundance of holes distributed in a network. This configuration makes possible to select certain incident photons and to filter scattered rays that disturb the image formation. The barriers that confine those holes are named collimator septa. The septa must be thick enough to absorb most of the photons incident upon them. Therefore, collimators must have thicker septa for higher energy photons. Modifying a collimator should involve a compromise between spatial resolution and efficiency, since the thickness of the collimator, the diameter of the holes and the septa thickness are directly related to the image quality obtained (21,22).

Multihole collimators differ mainly in their geometry. The holes may be hexagonal, square or triangular, however, most state-of-the-art collimators have hexagonal holes and are usually made of lead foil. Besides, they can also be distinguished by the alignment of the holes in a parallel, converging and diverging manner (**Figure 6**) (17,21).

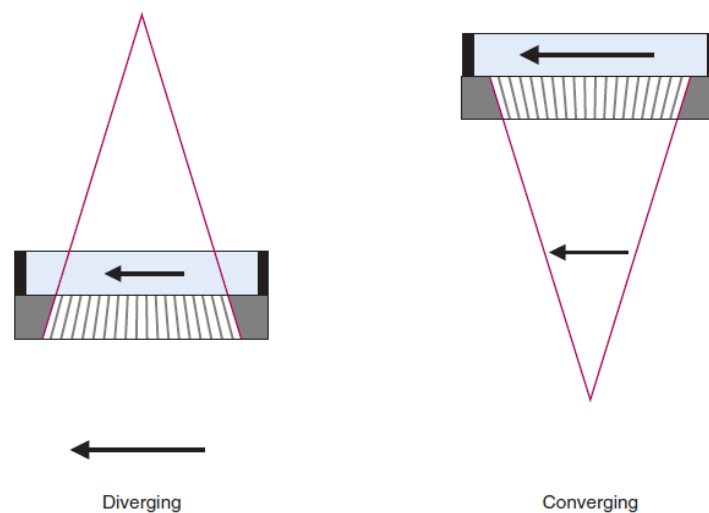


**Figure 6 - Diverging and converging gamma camera collimators (21).**

The parallel-hole (**Figure 7**) is the most widely used multihole collimator, which consists of an array of parallel holes essentially perpendicular to the plane of the scintillation crystal, presenting a real-size image to the detector (orthogonal geometry). The type of parallel-hole collimator should be chosen according to the energy of the isotope being imaged: low energy (up to 150keV), medium energy (up to 280keV) and high energy (up to 364keV) (17,20).

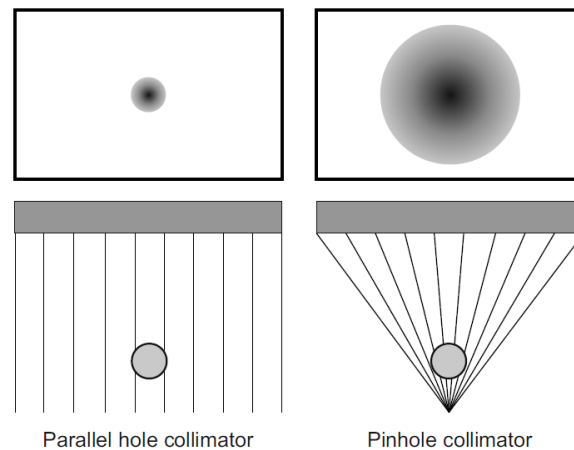


**Figure 7** - Main collimator configurations and their effect on the acquired image (16).

The pinhole collimators are thick conical collimators with a single hole in the bottom centre, based on the obscure camera in which light rays pass through the pinhole aperture and are projected to form an inverted image on the scintillation crystal (**Figure 7**). Since the radiation pass through a small aperture, only a small percentage of the emitted photons can reach the crystal, resulting in reduced sensitivity. Another disadvantage of the pinhole is the distortion that occurs due to the finite size of the hole (20,22).

The pinhole collimators are routinely used for images requiring high resolution such small organs like the thyroid and certain skeletal regions (hips or wrists) as a result of the possibility of magnifying and improving spatial resolution (17,22).

#### 2.1.1.2. Scintillation Crystal

The scintillation crystal is another component of a gamma camera, consisting mainly of a crystal of thallium activated sodium iodide, NaI(Tl). It is surrounded by a highly reflective material that is intended to maximize the light output, having also a thin aluminium casing for hermetical sealing. Despite the numerous available options, NaI(Tl) remains the crystal of

choice for single photon detection with energies of 70-360keV. Originally, the crystals had a circular cross section, but currently most cameras use a rectangular crystal 30-50cm wide and 0.9-1.2cm thick (**Figure 8**) (15,16,19).

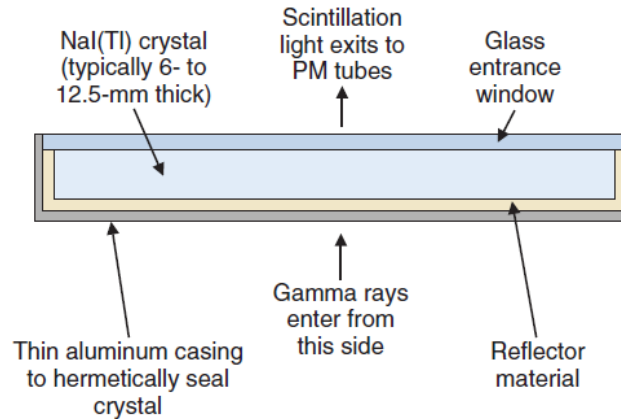


**Figure 8** - Schematic cross-section of a NaI(Tl) crystal for a gamma camera (21).

The purpose of a scintillator is to convert the gamma ray energy emerged from the patient into visible light after passing through the collimator. When ionizing radiation interacts with a scintillator, electrons are raised to an excited energy level. These electrons will then fall back to a lower energy state, producing a pulse of fluorescent light. The amount of light generated is directly proportional to the intensity of the absorbed energy, depending on the characteristics of the material (17,21).

Thus, scintillation materials must have specific proprieties such (21):

- High fraction of deposited energy that is converted into light - conversion efficiency;
- Short decay time, so the light can be emitted promptly after an interaction;
- Transparency to its own emissions to avoid reabsorption of the emitted light;
- Large attenuation coefficient to improve detection efficiency (materials with higher densities and atomic numbers).

Clinical Nuclear Medicine cameras are built with organic scintillators because of their high detection efficiency for the gamma rays. The advantages of NaI(Tl) are: a very high conversion efficiency (around 13%), reasonable decay time (230nsec) and inexpensive production in great quantities (large crystals can be manufactured). However, it is a fragile and hygroscopic material which needs to be hermetically sealed in airtight containers, making this its main disadvantage (19,21).

Although the energy resolution of a gamma camera is determined by the whole system, the light yield of the scintillation crystal is very significant, because it can improve the image contrast. The energy resolution expresses the ability of the detector to differentiate between gamma rays of closely spaced energies. NaI(Tl) has a moderate energy resolution, which is an important propriety that provides the means to discriminate against scattered radiation (15,19,22).

### 2.1.1.3. Photomultiplier Tubes

Having scintillation photons is not enough for the image formation. Thus, scintillation detectors incorporate a means of signal amplification that converts those photons into an electronic signal. This is accomplished by electronic devices referred as photomultiplier tubes (PMTs) (21,23).

Gamma cameras have an array of these devices located behind the scintillation crystal. They collect the light generated in the crystal, giving rise to electrical signals that contain information to determine the energy and position of interactions taking place in the crystal. Those interactions are processed individually, which requires the use of fast electronics and low dead time in the detector to allow high counting rates (22,23).

The number of PMTs is very important for the accurate localization of scintillation events, because the source can only be accurately tracked when considering the signals from other surrounding PMTs. Thus, the greater the number of PMTs, the greater the resolution. Moreover, the thickness of the crystal must be suited, because if the source is located far from the PMT (thicker crystals) the signal is weak and the location is not certain, degrading the spatial resolution (15,16,22).

The main components of a PMT are: the photocathode, a focusing grid, several dynodes with a high voltage supply and the anode (**Figure 9**).

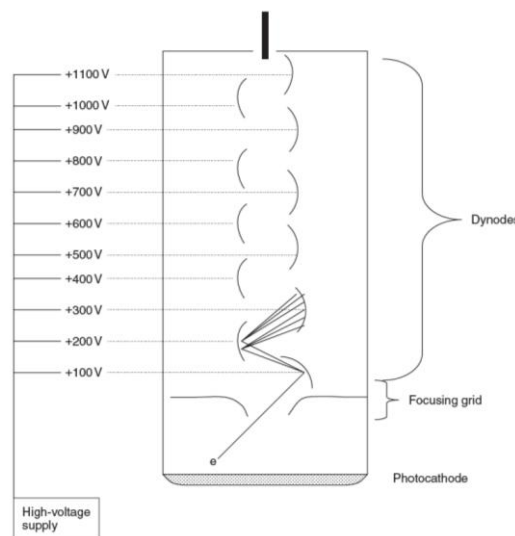


**Figure 9** - Basic structure of a photomultiplier tube (18).



The photocathode is near the window of the PMT and converts scintillation photons into electrons. It is made of a photo emissive material, usually metal alloys that have extra electrons that will be released into the vacuum space of the PTM when interacting with scintillation photons.

The focusing grid will then accelerate the electrons toward the first dynode.

A series of dynodes multiply the electrons generated at the photocathode into a measurable electronic signal. They are also made of metal alloys, each one with higher potential than the last, emitting electrons toward each other.

At last, the anode collects the produced electrons from the final dynode and gives off a voltage signal (22,23).

#### 2.1.1.4. Associated Electronics

When a gamma ray interacts in the scintillation crystal, scintillation photons are emitted. Those, in turn, cause the emission of a few electrons at the photocathode of the PMT that will be converted to a measurable electronic signal at the anode of the PMT. Although the signal given off by the PMT anode is measurable, it is considered small. Thus, a preamplifier and an amplifier are used to increase the output signal by a variable amount. Besides, they are also useful to shape and shorten the pulse in order to provide a series of discrete pulses that is easier to analyze (21).

The PMT signals are converted into a numeric magnitude by analog-to-digital converters, so that the energy and positions can be calculated by computer algorithms that can accurately model those signals with the source position (**Figure 10**) (19).

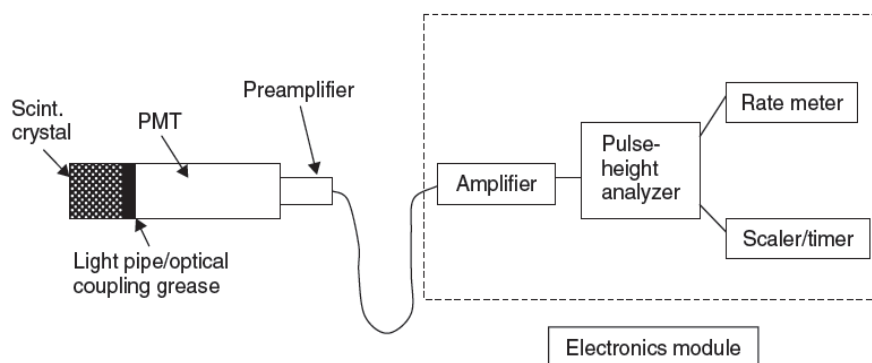


**Figure 10** - Diagram of a scintillation detector with the basic structure of the signal acquisition module (18).

## 2.2. Measures of Performance

A scintillation camera has two types of measures of performance: extrinsic and intrinsic. Extrinsic measurements are calculated with the collimator attached to the detection system. On the other hand, if the collimator is not present, the measurements are called intrinsic. Extrinsic measurements give the best indication of clinical performance while intrinsic measurements are more useful to compare the performance of different cameras (15).

### 2.2.1. Resolution

Resolution is one of the common performance parameters for gamma cameras. It can be referred as spatial or energy resolution (17,21,23):

- **Spatial resolution** is a measure of the ability of an imaging device to separate objects close together in space. It reveals the accuracy of the system to depict spatial variations in activity concentration and to distinguish as separate radioactive objects in close proximity;
- **Energy resolution** is the ability to discriminate between light pulses induced by gamma photons of differing energies. It evaluates how well a detector distinguishes between gamma rays of closely spaced energies.

Resolution can be increased by using more, smaller holes or by making the collimator longer. This will, however, reduce the fraction of photons detected by the system due to the increased amount of lead in the collimator (20).

### 2.2.2. Sensitivity

This parameter is defined as the overall ability of the system to detect the radioactive emissions from a source. Thus, it increases with the fraction of the emissions that are detected. Sensitivity can be increased for multihole collimators by increasing the size or shortening the length of each hole. However, this will occur at the expense of resolution. Thus, a balance between these two parameters needs to be done (20).

### 2.2.3. Uniformity

It is the quantity that measures the response of the camera to uniform irradiation of the detector surface, according to the uniformity of the obtained image. Field uniformity is

tested intrinsically and extrinsically. The intrinsic measurement is performed using a point radionuclide source in front of the camera without collimators, whilst system uniformity is assessed by placing a uniform planar radionuclide source in front of the collimated camera. The acquired images are then quantitatively analyzed by a computer in order to obtain the results (17,21).

#### **2.2.4. Dead Time**

If scintillation events occur too close together in time, the electronic system can be unable to count all the events that reach the crystal. The time after an event during which the system is unable to respond to another event is referred as the dead time, being strongly related to the count rate of the detector (24).

### **2.3. Bone Scintigraphy**

Bone scintigraphy or SS is one of the most common procedures in routine Nuclear Medicine. It is a diagnostic study that aims the evaluation of the distribution of active bone formation within the body (25,26).

With this technique is possible to obtain whole-body or limited bone scintigraphic images, according to the indications for the examination. In whole-body procedures, planar images of the entire skeleton are acquired, including anterior and posterior views (22).

The radionuclide bone scan is an extremely sensitive method for demonstrating a variety of skeletal disorders, allowing earlier diagnosis or demonstrating more lesions than conventional radiological techniques. The main indications for referral are: detection and follow-up of metastatic disease, trauma difficult to access on radiographs, sport injuries, evaluation of prosthetic joints and rheumatologic disorders (24).

#### **2.3.1. Radiopharmaceutical – $^{99m}\text{Tc}$**

Technetium (Tc) is a transition metal that, in the form of one of its isotopes Tc-99m, is the most widely used radioisotope in Nuclear Medicine. It has a half-time period of 6 hours, where 87% of the decays produce 140keV gamma photons (**Figure 11**). This property makes  $^{99m}\text{Tc}$  suitable for imaging with gamma cameras, being also safe regarding the patient's radiation dose (17).

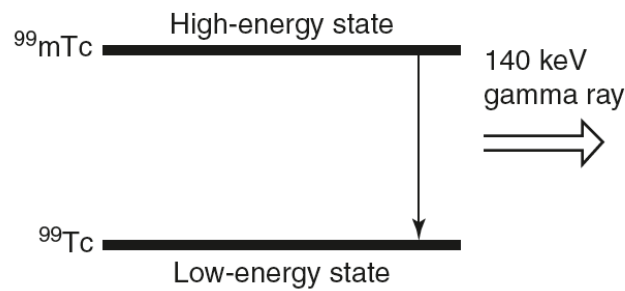


**Figure 11** - Gamma ray production. The atom passes from a high-energy state to a low-energy state, releasing a gamma photon with a peak energy of 140keV (27).

At the present, phosphate analogues labelled with  $^{99m}\text{Tc}$  are the radiopharmaceuticals of choice for SS. They are widely used on account of the good localization in the skeleton as well as the rapid clearance from soft tissues. Thus, they can provide a better image of bones due to the lower blood and tissue concentrations, giving a higher ratio of bone to tissue (25,28).

### 2.3.1.1. Mechanism of Accumulation

Two major factors control the accumulation of the radiotracer in the bone, specifically blood flow and extracting efficiency. The average administered activity for a single injection should be around 500MBq, corresponding to an effective radiation dose of approximately 3mSv. The uptake of any agent in the body depends on the blood supply, the capillary to bone transfer and the degree of osteoblastic and osteoclastic activity. After the radiopharmaceutical injection, about 50% of the activity accumulates in the skeleton according to the following steps (17,25,28,29):

- Generally, the clearance of  $^{99m}\text{Tc}$ -labeled radiopharmaceuticals from the vascular compartment is fast, with half-times of 2-4 minutes;
- The peak uptake in the bones is variable, but is normally reached at 1 hour after injection;
- The bone to background ratio varies with the different clearance and uptake rates of other tissues, having its maximum later at 4-6 hours;
- The combination of contrast, rapid renal excretion, peak uptake, radionuclide decay and practical issues, results in optimal imaging 2-4 hours after tracer injection. At this time, about one third of the administered dose is bound to bone.

### **2.3.1.2. Patient Preparation**

There is no special patient preparation concerning the bone scintigraphy. At the beginning, patients need to have a complete understanding of the procedure, including the reason of the delay between radiopharmaceutical administration and scanning, which is approximately 3 hours to achieve good bone accumulation and a low soft-tissue level of the radiopharmaceutical (23).

Unless contraindicated, patients should be well hydrated, being instructed to drink water between the time of injection and the time of delayed imaging. It will aid the clearance of the radiopharmaceutical from the body. Furthermore, voiding frequently is also important to reduce the radiation dose to the bladder and the activity on the bladder during the exam. Thus, the patient should also be requested to urinate immediately before the scan. During this phase, contamination with urine must be avoided, because it can lead to false-positive findings on the study (24).

It is also essential to remember that before considering submit a patient to a scintigraphic procedure, some precautions need to be taken: in case of pregnancy, a clinical decision is necessary to weigh the benefits against the possible harm; breast-feeding should be discontinued at least for 4h and for 24h post injection when possible (23).

### **2.3.1.3 Imaging Metastatic Disease**

The ability to image the entire skeleton makes planar bone scan unique when compared with other diagnostic techniques, resulting in a fast, cost-effective survey of the skeletal system. For this reason, the standard technique of bone scintigraphy in oncology is considered to be the whole-body scan. The overall sensitivity for detecting bony metastases is 95%, with a false-negative rate of 2% to 5% (28,30).

In the evaluation of oncological patients, SS provides the essential information related to the sites of osseous metastases, their prognosis and evaluation of osseous tumour response to chemotherapy and radiation therapy (25).

Many patients with known neoplasms and bone pain have metastases documented by the bone scan. Regardless, is also very important to scan patients with asymptomatic tumours that have a propensity to metastasize to bone, such as breast, lung and prostate carcinomas. For this reason, most patients are submitted to a whole-body scan within 6 months to 1 year, so that the extent of bone anomalies can be identified and compared in successive examinations. However, some variations may occur, modifying the conditions of the procedure throughout the series of scintigraphic scans (17,31).

Most metastases are multiple and relatively obvious but the interpretation may sometimes be difficult because of the single lesions, which have high false-positive rate. In general, bone metastases are observed as an increased uptake. The inherent osteoblastic response induces the deposition of radiotracer, generating a positive finding on the image. The usual pattern of metastatic bone disease is multiple focal lesions all over the skeleton, with the greatest involvement usually in the axial skeleton. Despite the high sensitivity of this technique, tracer uptake in bone scan is not specific for most metastatic bone disease (4,8,10,20,29).

Since metastases are usually located in the bone marrow, it is not the metastasis itself that shows up on the bone scan, but the reaction of the bone to the expanding malignant bone marrow. The lesions have cold signal when they are highly aggressive with fast expanding, since there is not enough time for the bone to respond and the regional blood flow may be damaged to such extent that the tracer cannot be delivered (26).

If a diffuse involvement of the skeleton by metastases is noticed, it may initially appear as though there has been remarkably good, relatively uniform uptake in all bones. This occurrence is commonly known as a *superscan*. If this finding is induced by metastases, a significantly decrease renal activity with diffusely increased activity will be noted throughout the axial skeleton. This condition is commonly a result of prostatic cancer, but other tumours such breast cancer and lymphoma may also be the source of this appearance (24).

Follow-up scans of advanced breast and prostate cancer should be interpreted with caution. When imaging bone tumour response on a planar bone scintigraphy, findings usually emerge as a decreased intensity of radionuclide uptake by the metastatic foci. However, in the first 3 months of chemotherapy, a favourable clinical response by focal bone metastases may result in healing and increased uptake, which is a good prognostic sign. Disease progression is usually suggested by bone lesions that appear 6 months or later after treatment (24).

#### **2.3.1.4. Imaging Technique**

According to the procedure guidelines of the European Association of Nuclear Medicine (EANM), image acquisition for bone scintigraphy should be performed using a single or a double-head gamma camera, equipped with a low-energy, high resolution collimator, which is suitable for the 140keV photopeak of  $^{99m}\text{Tc}$  (23).

In adults, whole-body bone scintigraphy is performed with continuous imaging, obtained in both anterior and posterior views. Routine images of the skeletal phase are usually acquired between 2 and 5 hours post-injection, where the scanning speed might be adjusted with the purpose of obtaining more than 1.5 million counts in each routine image view. For a routine study, the average procedure imaging time is about 30 minutes (26,28).

## 2.4. Pitfalls and Artefacts

There are several sources of error in bone scintigraphy. They can be artefacts related to the patient or to the technique itself.

Technical artefacts include equipment, radiopharmaceutical and image processing problems due to (28,32):

- Poor quality control and calibration;
- Inadequate preparation of the radiopharmaceutical that modifies biodistribution and compromises the diagnostic quality of the images;
- Extravasation at the site of injection, the most common artefact on bone scintigraphy;
- Source-to-detector distance greater than necessary;
- Imaging at wrong timing.

The main patient-related artefacts can be described as (28,32):

- Patient movement;
- Urine contamination;
- Prosthetic implants or other attenuating artefacts that may obscure normal structures, inducing photon-deficient areas;
- Homogeneously increased bony activity;
- Restraint artefacts caused by soft-tissue compression;
- Pubic lesions obscured by underlying bladder activity;
- Renal failure.

Moreover, there are several pitfalls that can originate misinterpretations of the image findings (28):

- Some aggressive or purely lytic metastases may not produce a visible osteoblastic response. Thus, they will appear as purely cold lesions, making more difficult their identification on a routine whole-body bone scan;
- If the bone scintigraphy is used for the assessment of treatment response but performed very soon after the treatment, it may be difficult to differentiate a flare response from tumour progression;
- When patients have undergone recent surgery such knee or hip replacements, bone scintigraphy may give false-positive results if performed too early. Thus, a later date for the examination can be considered. Otherwise, caution in the interpretation is required.

### 3. Reducing Scan Time in Bone Scintigraphy

To generate an adequate diagnostic image in Nuclear Medicine, an appropriate balance between image quality and radiation dose is required. According to this, it is desirable to reduce radiation dose as well as the scanning time. For clinical practice it is important to obtain an accurate clinical diagnosis with collection of a minimum number of counts (33).

Since Nuclear Medicine images suffer from relatively high levels of noise and low SNR. Noise reductions can be achieved by increasing radiation dose or image acquisition times or even by filtering the image with processing and post-processing techniques. Thus, some practical steps can be considered to improve diagnostic values in Nuclear Medicine diagnostic imaging (27,34,35,36):

- **Radiopharmaceutical dose:** As mentioned above, an accurate diagnosis suggests using the minimum radiopharmaceutical dose, suitable for each procedure (particularly in the case of repetitive imaging). This means that reducing the administered radiopharmaceutical will generate images with decreased SNR. On the contrary, despite the fact that increasing the administered radioactivity increases the number of counts in the image, it could lead to higher radiation dose to patients;
- **Pixel size:** A digital image is one in which events are localized (or “binned”) within a grid comprising a finite number of discrete picture elements referred as pixels. For a gamma camera, the detector area is divided into the desired number of pixels, where each pixel corresponds to a range of possible physical locations within the image (**Figure 12**). Digital images can be characterized by their matrix size, which is the number of pixels presented by the image matrix. This parameter affects the degree of spatial detail that can be presented, with larger matrices (smaller pixel size) providing more image detail. On the contrary, increasing pixel size could lead to noise reduction with increased SNR, but it would also induce reduced resolution due to the smaller amount of collected signal;

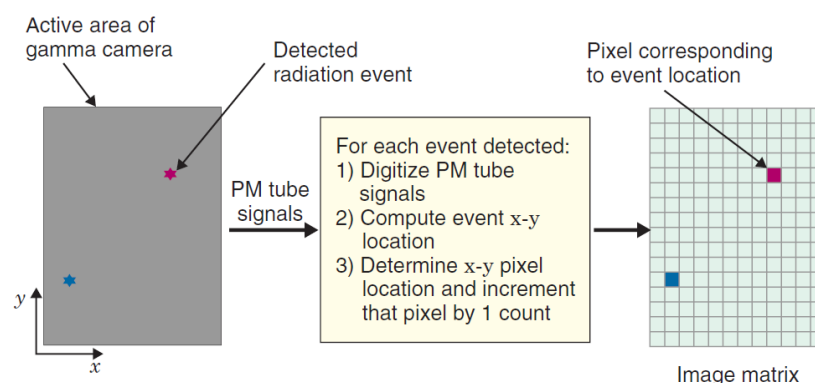


**Figure 12** - Subdivision of the gamma camera detector area for generating a digital image (21).



- Acquisition time: Extending the duration of the procedures increases the number of collected counts. However, this is not tolerated by many patients and this could also result in the appearance of motion artefacts since patients have tendency to move when experiencing discomfort, due to pain for example. In this field, there is always a compromise between image quality, workflow economics, patient safety and patient comfort;
- Reconstruction methods: An alternative option is to apply reconstruction techniques that allow increases in spatial resolution, enhancing the signal. However, this process is highly influenced by noise due to random measurement errors, which cannot be predicted. Thus, one needs to assume that they are random realizations of some parental statistical distribution in order to find a solution for the image model. Moreover, noise effects can be reduced by using appropriated techniques for statistical filtering.

Digital image processing makes possible to reconstruct images acquired from non-ideal conditions, obtained from real-world instruments. As a result, information present but hidden in the data can be revealed with less blur and noise. This means that low-count, noisy images can have their quality improved, allowing images with a lower number of counts to be acquired (37,38).

Presently, the pressure to reduce injected activities has reached new levels, making more rapid scanning desirable as well. Besides, due to their debilitating condition, patients submitted to whole-body bone scans can experience pain and anxiety during the examination. Because of the long scanning times in use for standard procedures (about 30 minutes) it is even more difficult to acquire images with sufficient image quality (33).

Thus, the reduction of acquisition time together with suitable image processing methods may be an appropriate method for noise reduction. Hence, the best technique must be found in order to increase confidence in the diagnosis of features observed in the image originally acquired with modified parameters (29).

## **4. Processing Scintigraphic Images**

Digital image processing is a robust means by which the underlying images hidden in blurry and noisy data can be revealed. It has been widely developed, providing high-quality reconstructions of blurry and noisy data collected by an extensive variety of sensors. Thus, it is mathematically possible to reconstruct the underlying image from non-ideal data collected from real-world mechanisms, so that the hidden information can be revealed with less blur and noise (38,39).

The use of digital processing techniques can be used for image improvement, having many applications in space imagery and medical research. It involves operations that improve the quality of an image as perceived by a human or a machine, applying a broad set of algorithms and tools to repair, analyze, develop and visualize images. The need for implementation of image processing techniques will depend on the physical properties of the systems that describe their quality of response (22,39).

### **4.1. Image Quality in Nuclear Medicine**

Image quality can be defined by the capability of the system to detect relevant information, being related to the accuracy with which an image represents the imaged object. The quality of medical images depends on its information content and how accessible the information is, defined as its usefulness in determining an accurate diagnosis. As mentioned in the previous chapter of this document, there are several concepts used to describe imaging systems in terms of their quality of response, being referred as spatial resolution, contrast and noise. Those parameters are also recognized as the essential elements of image quality in Nuclear Medicine, being related to the diagnostic utility of the image (21,22).

Despite the fact that the mentioned characteristics used for Nuclear Medicine image quality describe three different aspects, they cannot be treated as completely independent parameters, because improving one of them may induce deterioration of one or more of the others (21).

There are two main limitations in image accuracy: blur and noise. Blur is intrinsic to the image acquisition systems, because digital images have a finite number of samples. On the other hand, noise is related to the fluctuation that occurs in each pixel when receiving a certain number of photons from a particular source. This means that the number of photons received fluctuates around its average, in accordance with the central limit theorem (30).

#### 4.1.1. Spatial Resolution

Spatial resolution is a property that describes the ability of an image system to accurately depict objects in the two or three spatial dimensions of an image. Technically, the spatial resolution of a digital image is regulated by two factors: the resolution of the imaging device itself and the size of the pixels used to represent the image in its digital format. Consequently, despite the higher amounts of noise, a smaller pixel size can exhibit more image detail. However, beyond a certain point there are resolution limitations related to the imaging device, allowing no further improvements on the acquired image (21,28).

Nuclear Medicine images have somewhat limited spatial resolution, at least when compared with radiological images. As mentioned in the previous chapter of this document, a number of factors contribute to the lack of sharpness in these images (21).

The evaluation of spatial resolution can be performed by subjective or objective means. A subjective evaluation involves visual inspection of the images. However, different observers may provide different interpretations, making the estimation of image quality difficult and subjected to inter-observer variability. One conceptual way of understanding and measuring the spatial resolution of a detector system in the spatial domain is to stimulate the detector with a single point source and then observe the way it responds (21,27).

#### 4.1.2. Point Spread Function

The image produced by a detector system from a single point input is referred as the point spread function (PSF). It expresses the blurring properties of the imaging system, describing the imaging system response to a point input (**Figure 13**).

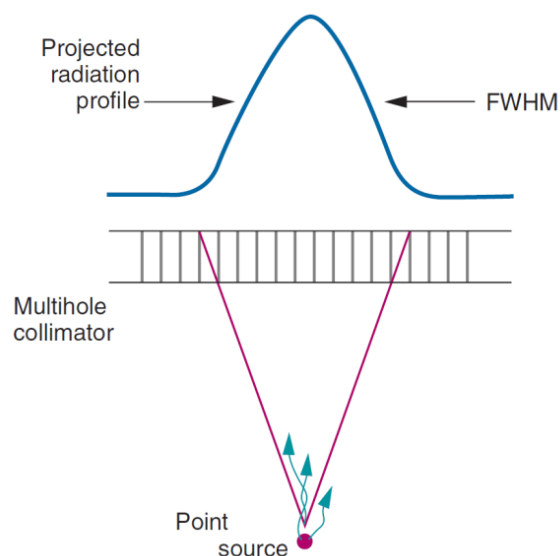


**Figure 13** - Radiation profile (PSF) and relative FWHM for parallel-hole collimator (21).

The full width at half maximum (FWHM) of the generated profile is used to characterize the collimator resolution. Because PSF's of different shapes can have the same FWHM, it only provides a partial specification of the spatial resolution characterization. However, the FWHM is considered as an useful parameter for general comparisons of imaging devices and techniques (21,27).

On other words, the PSF expresses the performance of medical imaging devices in terms of sensitivity and spatial resolution by means of a function that describes the image when the object is a point. It describes how a photon originating at position  $y$  in the image plane ends up at position  $x$  in the focal plane. In general, the PSF varies independently with respect to both  $x$  and  $y$ , because the blur of a point source can depend on its location in the image (22,28).

#### 4.1.3. Signal-to-Noise Ratio

The signal-to-noise ratio is an expression used to describe the power ratio between the signal (significant information) and the background noise. In one imaging application view, these quantities would be a fixed known activity concentration and the standard deviation of its inherently fluctuating measured values attributable to the imaging protocol (31).

Thus, measuring the amount of noise by its standard deviation,  $\sigma(N)$ , one can define the SNR as (30):

$$SNR = \frac{\sigma(U)}{\sigma(N)} \quad (1)$$

#### 4.1.4. Contrast

Image contrast can be described as the ratio of signal change of an object of interest, relative to the signal level in surrounding parts of the image. It is related to the intensity differences in parts of the image corresponding to different levels of radioactive uptake in the patient. In Nuclear Medicine, a major component of image contrast is determined by the properties of the radiopharmaceutical. Image contrast is also affected by the physical factors involved in image generation for being related to the statistical noise levels in the image, affecting the contrast-to-noise ratio (21).

#### 4.1.5. Noise

A common form of noise consists of significant undesirable random fluctuations in pixel values that are superimposed on the ideal true values associated with objects being viewed. This phenomenon is commonly due to the random nature of the detection process and is visually perceived as graininess (31).

On a first approximation, one can write the acquired image in the following form (30):

$$D(i) = U(i) + N(i) \quad (2)$$

Where  $D(i)$  is the observed value,  $U(i)$  would be the “true” value at pixel  $i$ , namely the one which would be observed by averaging the photon counting, and  $N(i)$  is the noise perturbation. The last parameter corresponds to small random pixel variations in the value superimposed on a true mean value from uptake signal (40,41).

Images may be subjected to noise and interference from several sources. It can be caused by the randomness in the radioactive process as well as by some features of image reconstruction. Consequently, it creates problems for the subsequent process of reading and interpreting such images. Noise effects can be reduced by statistical filtering techniques or by a different approach, the application of noise cleaning techniques. However, image noise reduction (denoising) has remained a main problem in the image processing field (39,42,43).

The main challenge is sensitivity to noise measurement in the input data, which can be strongly magnified, resulting in large artefacts in the reconstructed image. The answer to this difficulty is to restrict the permitted images. Progressively most sophisticated restrictions have been developed, imposing a variable degree of restriction across the image. However, the most consistent reconstruction method is considered the most conservative one, which restricts the permissible image modules (32).

Modern image reconstructions differ only in what they restrict and how they implement the restriction. The more restrictive the image reconstruction, the greater the stability, however, more likely will be to eliminate correct solutions. Thus, imposing the maximum, spatially adaptive smoothing allowed by the data results can be the best image reconstruction technique, in which the aim is to be as close as possible to the true underlying image. Accordingly, the goal is to describe the allowed solutions in a sufficient general way that includes all the possibilities, confining the results to the preferred images (32).

## 4.2. Image Reconstruction

The massive production of digital images has widely increased the need for efficient image reconstruction methods. Since images are often generated in poor conditions, an image improvement is always desirable (30).

Image reconstruction for data acquired with linear detectors often becomes a matter of inverting an integral relation of the form:

$$D(x) = \int dy H(x, y) I(y) + N(x) \quad (3)$$

Where:

$D(x)$  – Array of data points;

$H$  – PSF;

$I$  – Required underlying image model;

$N$  – Noise.

In general, the imaging problem may be defined in a space with an arbitrary number of dimensions  $(x, y)$ . If  $H(x, y)$  is the PSF for a 2D imaging system and is symmetric about a central axis, the response of the system can be totally described by the curve  $H(x)$  in an axial plane that intersects  $H(x, y)$ . The system sensitivity will be proportional to the volume under the surface  $H(x, y)$ . A perfect imaging system presents a point for each object point, meaning that the response is ideal (17).

There are two major problems when reconstructing images: noise fluctuation and overinterpretation of data. Image reconstruction differs from standard solutions of integral equations due to the noise term,  $N$ , whose nature is only known statistically. Moreover, noise fluctuations may be mistaken with real signal. Thus, specific methods for the reduction of random noise in planar images subject to noise statistics must be implemented (36,38,44).

At present, several advanced image processing techniques have been developed seeking the enhancement of digital images through reconstruction methods. The method of interest for this research will be the EPP implementing the Pixon method (37).

## 5. Pixon Method

The Pixon method represents an innovative way of modelling an image in terms of its information content, allowing new competences in the fields of image reconstruction and data compression. As it offers versatile commercial software for a wide range of applications together with strong benefits to all kinds of imaging systems, the areas of medical imaging are not an exception (34).

Since image reconstruction is an important application in a number of fields, the Pixon method promotes medical images enhancement by (37):

5. Improving sensitivity, reducing false negatives;
6. Eliminating image artefacts, reducing false positives;
7. The reduction of patients risks from ionizing radiation;
8. Reducing effects due to patient motion by reduction of image acquisition time;
9. Reducing total cost of medical care.

The Pixon method is a high-performance image reconstruction technique that searches for the smoothest image statistically consistent with the raw counts. This concept was developed by Pina and Puetter in 1993 to restore astronomy images, with the purpose of eliminate problems with existing image reconstruction techniques, particularly signal-correlated residuals (**Figure 14**). The goal of this technique is to construct the simplest model for the image that is consistent with the data. As it is the simplest model, the derived image would be artefact free with no spurious sources. Consequently, Pixon method seeks for minimum complexity for the plausible model of the image, which enables an efficient representation of the image as well as the best way to separate signal from noise. It has been applied to many fields, including medical image reconstruction (44-48).

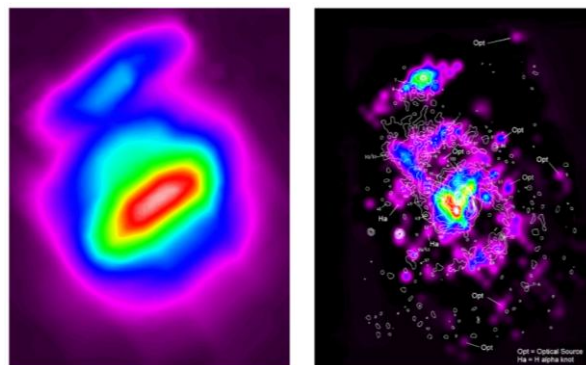


**Figure 14** - Pixon reconstruction of a satellite survey scan. The resolution of the reconstructed image (on the left) is 20 times finer than the raw scan (on the right) and the sensitivity is improved by a factor of 100 (34).

The Pixon concept is based on a nonlinear image reconstruction algorithm that increases linear spatial resolution by a factor of a few and sensitivity by an order of magnitude or more. Linear processing techniques are applied on images with continuous noise, however, they tend to provide too much smoothing. Despite the fact that they are more compact and less computationally demanding, they have poor noise propagation properties. In contrast, nonlinear techniques have been considered as the most successful modern methods of image reconstruction. This method is more complex, however, it often provides a better trade-off between noise smoothing and retention of fine image detail due to better control over the propagation of noise (39,44,49).

Pixon noise-reduction method provides statistically unbiased photometry, since it performs a robust rejection of spurious sources by using the local information content, preserving statistically justifiable image features without generating artefacts. It can be applied on planar Nuclear Medicine images with known Poisson noise characteristics with the following goals: increase sensitivity for detection of lesions of decreased activity-to-background ratio; reduce acquisition time; and reduce patient dose (**Figure 15**) (29).

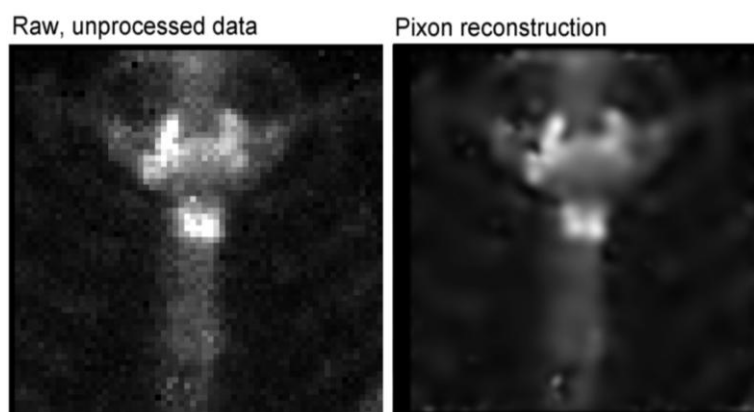


**Figure 15** - Pixon reconstruction of a digital Nuclear Medicine planar image. The raw image is significantly blurred with noise artefacts from photon counting statistics. On the contrary, the reconstructed image has improved resolution and reduced noise, enhancing the diagnostic capabilities (**34**).

Thus, image processing with Pixon is a method based on a process of spatially adaptive, minimal complexity image reconstruction. It aims to strip away the inherent noise observed in low- count images, seeking the simplest underlying true image that can fit the collected data. The model is necessarily the most tightly constrained by the data, and consequently has the most accurately determined parameters. Since this method has minimum complexity, spurious sources are unlikely to occur (**Figure 16**) (37,48).





**Figure 16** - Performance of the Pixon method for the “Lena” Matlab image (34).

Instead of representing the images with pixels of a constant size, Pina and Puetter introduced an image model where the size of the pixels varies locally according to the information density in the image, generally referred as pixons or degrees-of-freedom. Each Pixon represents a degree of freedom that is determined using a larger fraction of the data and so is determined more accurately. A map of the Pixon sizes is called an image model (**Figure 17**). With this, the Pixon method aims to find the best match between the image and its image model that is consistent with the data and can represent the structure in the image by the smallest number of pixons. This generally results in superior photometric and positional accuracy and, since the minimum number of parameters are used, the data cannot be over-fitted (48,50).

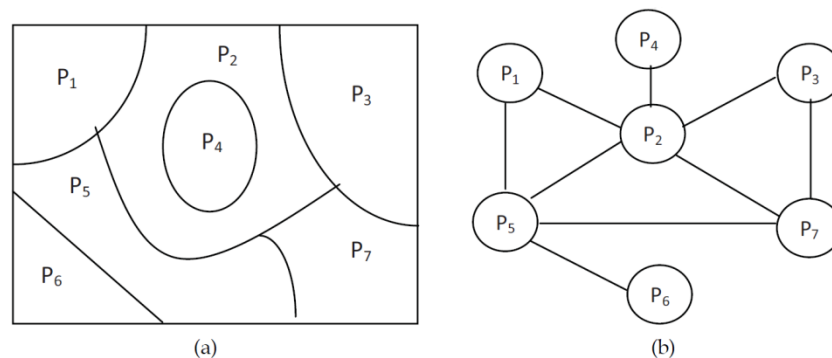


**Figure 17** - (a) - Example of a Pixon image model; (b) - Its correspondent graph structure (35).

According to the basis of Pixon-based method, images can be briefly described using a reduced amount of degrees-of-freedom where the image characteristics are smooth, and using more degrees-of-freedom where greater detail is present. Clearly, if the signal in the image can be adequately represented by a minimum number of parameters, adding another parameter will only introduce artefacts by fitting the noise. On the other hand, removing parameters results in an inaccurate representation of the image. Since the Pixon definition

scheme should yield an optimum scale description of the observed image, the ability to control the number of degrees of freedom used to model the images is the key aspect (44-46).

The procedure to determine the set of Pixon elements, specifically their shape and size, includes obtaining a pseudo image. The pseudo image is a basic representation derived from the observed image that has at least the same resolution as the original image. With this, the image model is made up contiguous and nonoverlapping cells, regarded as pixons, having constant intensity within each Pixon (**Figure 18**) (45,51).



**Figure 18** - Pseudo image and its correspondent Pixon map with the resulting reconstructed image. The Pixon map shows the spatial scale applied at each pixel, which represents where the information is concentrated (**36**).

In order to minimize complexity, the Pixon method smoothes the image model locally as much as possible, reducing the number of independent patches, the Pixon elements. The dimensions of the pixons define locally the scale of underlying image information. In fact, those elements describe directly the “natural graininess” of the information in a data set due to the statistical uncertainties in the measurements (44,46,52).

The description of an image’s set of pixons is highly idealistic. As a consequence, Pina and Puetter introduced two practical Pixon bases. The first scheme proposed was named Uniform Pixon Basis (UPB) in which the algorithm complexity for each Pixon was equal. The second scheme was called the Fractal Pixon Basis (FPB) and analyses the algorithm complexity of the image in terms of a single spatial scale, being referred as “fuzzy-Pixon”, which is a correlation approach where adjacent pixons share some of each other’s signal instead of having hard boundaries. In this approach, the independence of the different parts of the image is reduced through explicit spatial correlation, assuming an intrinsic correlation length that can vary across the image. Reconstructions using the FPB approach can be mentioned as the standard Pixon method. The reconstructed images have no signal-correlated residuals and are effectively artefact (false-source) free (**Figure 19**) (50,53,54).

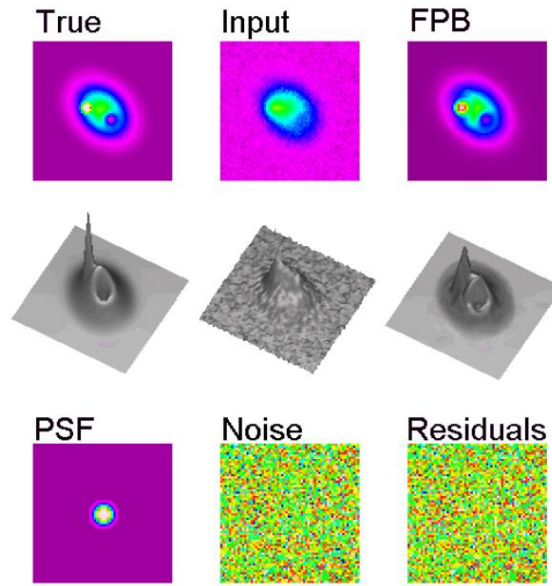


**Figure 19** - Pixon image reconstruction (FPB) for a synthetic data set for which the true (unblurred) image, the blurring function (PSF) and the input noise are known a priori. Top row (from left to right): true image, blurred and noised input data to the reconstruction and Pixon reconstruction; Middle row: surface plots of the top row images; Bottom row (from left to right): PSF, input noise and residuals for the Pixon reconstruction **(34)**.

Formally, the image is written as an integral over a pseudo image (38):

$$D(x) = \left( H * (K \otimes I_{pseudo}) \right) (x) + N(x) \quad (4)$$

Where:

$D(x)$  – Array of data points;

$H$  – PSF;

$K$  – Blurring function;

$I_{pseudo}$  – Pseudo image;

$N$  – Noise in the data;

$*$  – Normal convolution operator;

$\otimes$  – Local convolution or smoothing operator.

And  $I_{pseudo}$  is defined such that the normal image can be:  $I(x) = (K \otimes I_{pseudo})(x)$ .

The operator  $K$  transforms the underlying field to data space. For images, it is the PSF, typically blurring the image due to instrumental and possibly atmospheric blurring. To solve **Eq. (4)**, it is assumed that the functional form of the PSF is known, although it may have unknown parameters which need to be determined from the data. Moreover, the noise is taken to be sufficiently well understood since its nature is only statistically known (44,51).

The goal of Pixon image reconstruction is to find the smoothest possible image by selecting the broadest possible nonnegative, spatially variable kernel  $K$ , for which a nonnegative pseudo image  $I_{pseudo}$  can be found. As a result, the Pixon method starts with a finely sampled positive pseudo image and smoothes it with a positive kernel function to obtain the image. Thus, the method proceeds alternatively between determining  $I_{pseudo}$  and  $K$ , starting with the determination of  $I_{pseudo}$  with some initial  $K$ . Furthermore, the normal image is replaced by a pseudo image smoothed locally by a function with position dependent scale. The  $(K \otimes I_{pseudo})$  operator can then be referred as the sought underlying image model (38,51,53).

Thus, the Pixon reconstruction combines the search for the broadest possible kernel functions together with their pseudo image values that provide an adequate fit to the data, depending on the essence of the Pixon method applied (**Figure 20**) (39).

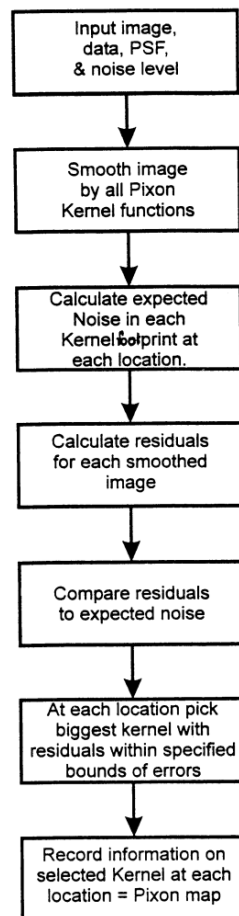


**Figure 20** - Block diagram of the steps of image reconstruction with Pixon map calculation (40).

Alternatively, the pseudo image can be solved with a given Pixion map of kernel functions and then attempt to increase the scale sizes of the kernel functions given the current image values. The required number of iterations depends on the complexity of the image, but for most problems a couple iterations is sufficient (**Figure 21**) (39).

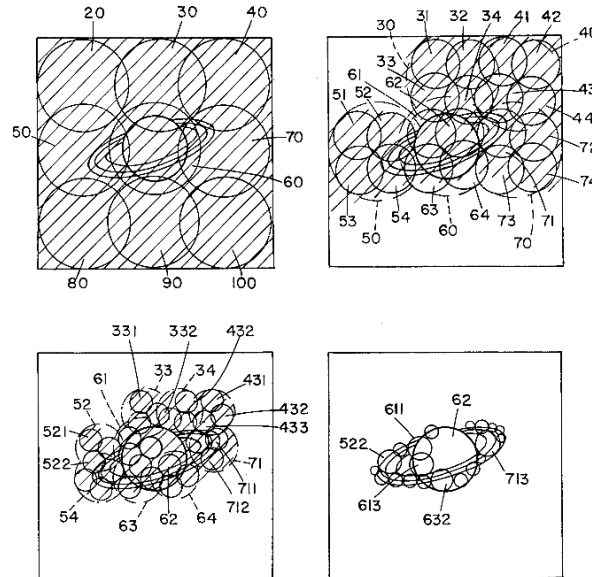


**Figure 21** - Simulated image reconstruction sequence using a multiresolution decomposition of the image model. Top row (left to right): noisy input data with a first iteration Pixion map; and second iteration with new smaller scales kernels. Bottom row (left to right): Third iteration Pixion map; and final Pixion map (**40**).

When the SNR is not too low, a Pixion reconstruction proceeds reasonably well, however, for lower SNR more elaborated methods are needed. In the case of gamma rays experiments with lower SNR, the derivation of the Pixion map requires mean field annealing which is a deterministic approximation for solving optimization problems, at higher computational cost. Efforts have been made to develop faster and more general techniques. This progress has already been achieved with the creation of a “black box” software which does not require fine adjustments by the user. Nowadays, this technology has been integrated in medical imaging systems and is available commercially for post-acquisition processing, but there are remaining uncertainties regarding diagnostic agreement that make its employment not widely accepted (37,51).

# **Enhanced Planar Processing in Clinical Practice**

## **6. Purpose of the Study**

Images obtained in Nuclear Medicine procedures can have high levels of noise, resulting in interpretation difficulties. Presently, improvement of image quality is possible through the application of image processing tools. As mentioned before, Pixon software is a suitable technique in which the Pixon method is applied so that images can be improved. This image processing method allows the enhancement of digital images by increasing the sharpness, suppressing noise and enhancing the contrast.

Since Pixon software can be integrated in specific imaging systems, Siemens (Siemens Medical Solution, USA) developed a software package for Enhanced Planar Processing using the Pixon method, in which a Whole-Body Enhanced Planar Acquisition protocol was included. According to Siemens, the referred technology enables the generation of reconstructing low count planar images of comparable quality in relation to images acquired using standard protocols. This is applicable when either reducing the acquisition time and/or administration of lower doses of radiopharmaceutical. Both methods can allow higher throughput within the department. Besides, less motion artefacts and/or lower radiation exposures can be achieved.

Recently, such software package became available at the Radboud University Medical Centre at the department of Radiology and Nuclear Medicine. However, there are still some uncertainties whether EPP affects patient diagnosis on planar images and eventually management of patients.

Thus, this study aims to assess the performance of an EPP algorithm in clinical practice regarding diagnosis and reader confidence, so that the safe employment of the software can be warranted.

Furthermore, this investigation will focus on oncologic patients, from breast and prostate carcinomas, particularly those with suspected bone metastasis. This particular choice was made, given that there are many previous studies indicating that the fraction of bone containing metastatic lesions related to prostate and breast cancer patients is a strong prognostic indicator of a long survival. In such patients, pain can be a major drawback when performing bone scintigraphy. For this reason, the objective is to reduce scan duration in 50% so that patient care can be improved, maintaining the same diagnostic quality of the examinations.

## 7. Materials and Methods

The present study was performed at the Radboud University Nijmegen Medical Centre, a leading institution for medical research and education, more particularly at the department of Radiology and Nuclear Medicine. This department provides state-of-the-art radionuclide imaging and therapy with radiolabeled tracers, being equipped with four gamma cameras and one PET-CT scanner.

During the investigation, all the gamma cameras available were used to collect the data since the intention is to validate the implementation of this technique in the whole department. Thus, the scans of interest for the study were performed in properly calibrated Siemens equipment, on either a Symbia S or Symbia T16 dual head gamma cameras.

The methodology of this study is summarized in **Figure 22** and all the steps are properly explained and described in the next topics.

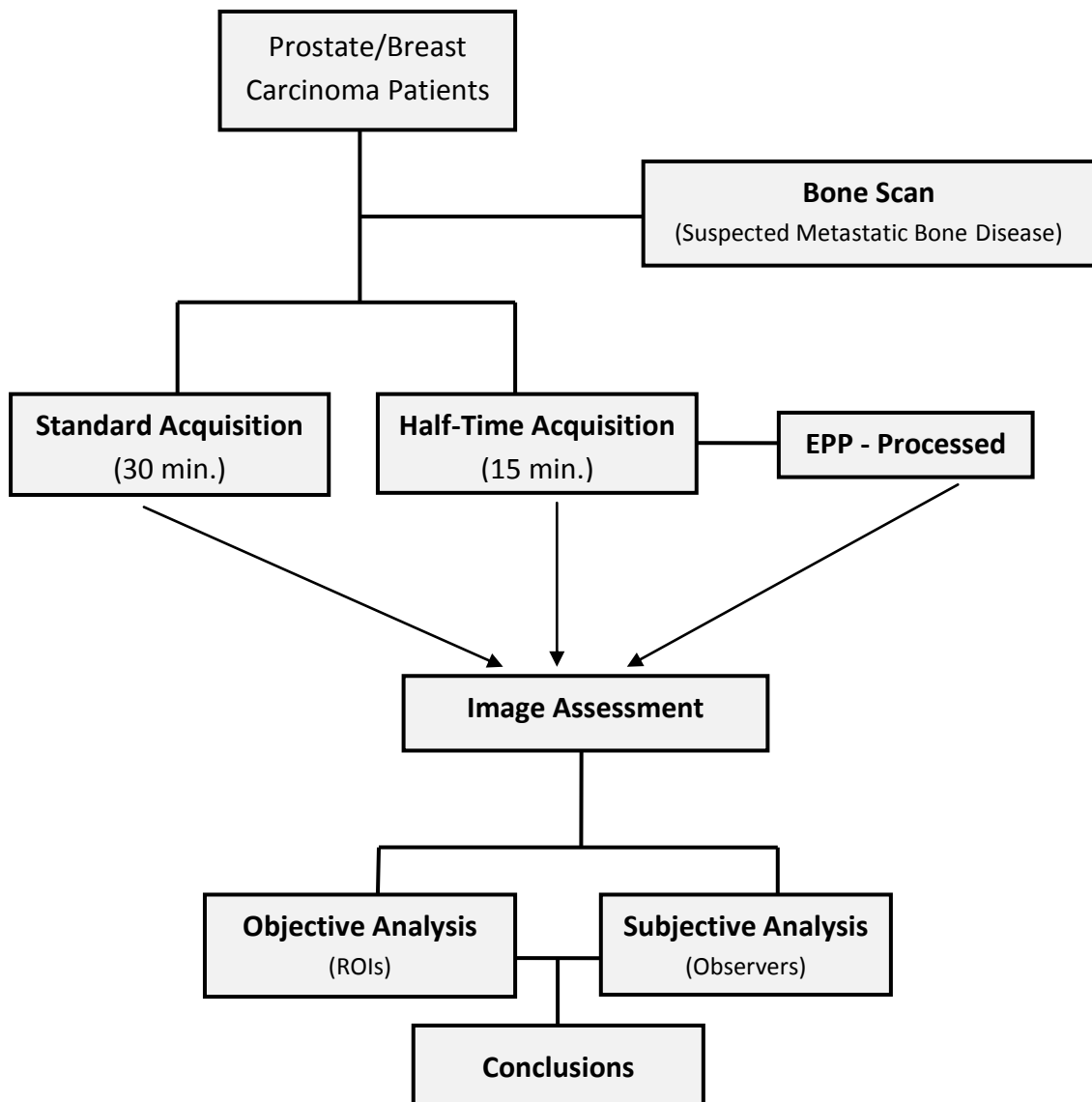


**Figure 22** - Scheme of the methodology used in this study.



## **7.1. Patient Population and Image Acquisition**

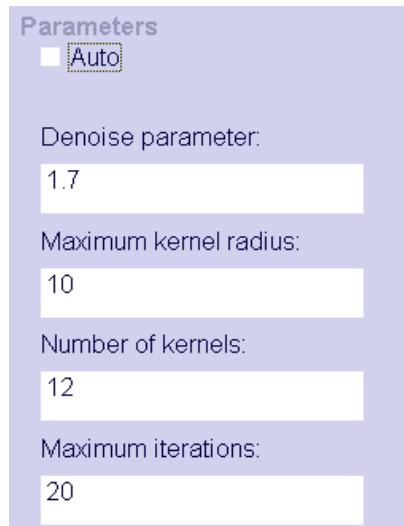
A total number of 51 adult patients were included in the study. Patients who had to be referred to bone scintigraphy due to suspected metastatic bone disease from prostate and breast cancer.

The patients received standard preparation for the bone scan, including the standard dose intravenous injection of 500MBq <sup>99m</sup>-technetium-labeled hydroxymethylene diphosphonate with 3 to 5 subsequent hours of incubation. After this period, the individuals went through two different scintigraphic whole-body bone scans: one acquisition with the standard clinical protocol (acquisition time of 30 minutes); plus another with 50% reduction in scan duration (acquisition time of 15 minutes). According to the Siemens recommendations for EPP employment, the maximum recommended count reduction resulting from reduced processing time should be a factor of two (half the counts).

Before the request for a second scan, the physical and mental conditions of the patients after the standard protocol were taken into account. If they were able to proceed for a second scan, the purpose and method of the study had to be explained so that informed consent could be obtained from the patients when they accepted to participate on the study.

Both performance results were acquired in anterior and posterior views, with the same camera parameters: matrix size of 256x1024; 1.00 zoom; using both detectors with low energy high resolution (LEHR) collimators. The only difference between the two performances were the finishing conditions of the examination table, with scan speed of 8cm/min for the standard performance (full-count acquisition) and 16cm/min for the half-time performance (half-count acquisition) (**Appendix I**).

After completion, the images acquired in the shortened scan needed to be processed. For this purpose, the software package for EPP available at the department was used. Using the Whole-Body Enhanced Planar Acquisition tool (**Appendix I**), the images were reconstructed, according to the parameters shown in **Figure 23**, so that image quality could be improved.



Parameters

Auto

Denoise parameter:  
1.7

Maximum kernel radius:  
10

Number of kernels:  
12

Maximum iterations:  
20

**Figure 23** - Reconstruction parameters applied in the Whole-Body Enhanced Planar Acquisition tool (Siemens Medical Solutions, USA).

## 7.2. Organizing the Collected Data

The step following the performances and reconstruction of the images was the organization of the data. A database with information regarding each individual included in the study was created.

In addition, a specific database was created in HERMES v. 4.6-A (HERMES Medical Solutions - Stockholm, Sweden), which is the software that is in use at this department for processing, archiving and distribution of medical images. Images in this database include standard, non-processed half-time and processed half-time images. Anonymous series were used in order to blind the readers to the image details, clinical indications, administered doses and the percentage of original counts in the images. Only the year related to the date of birth was maintained so that the image findings could be related to the age of the patients, reducing the probability of false positives associated to other bone conditions (**Appendix II**).

## 7.3. Image Assessment

In this investigation, two methods of image assessment were performed: a visual or subjective analysis and an objective analysis.

### 7.3.1. Subjective Analysis

Three Nuclear Medicine physicians (with 3, 5 and 6 years of experience) were presented with 153 images (full-count, half-count and Pixon-processed) from 51 patients, in a blinded randomized order, for an independent review. All images were viewed on the same type of diagnostic workstation and colour LCD monitor, under the same environmental lighting conditions. Besides, it is important to refer that the images from each patient were separately assessed in a blind evaluation.

Following the same protocol used in the clinical practice for the evaluation of scintigraphic bone scans, a printed version was generated for each image series using the Display and Scale tool on HERMES interface (**Appendix III**). A print consists of an image with the two views of the scan (anterior and posterior) doubled, in which a proper grey scale is defined for each pair of views. This means that each pair must have low and high contrast levels, respectively, for an accurate interpretation. This practice was also important since all images were created taking the standard print as reference, which was used for diagnostic purposes. This way, the appearance of the images was comparable in all the cases, reducing the probabilities of misdiagnosis.

The images (prints) from each study were presented to the physicians using a database in HERMES, which only included the created prints. They were requested to score the diagnostic quality of each performance by means of a simple scoring form (**Appendix IV**). The scoring form, which was previously discussed with the more experienced physician, was presented to each observer. The first question was whether the physicians diagnosed any visible lesions (yes/no) (**Figure 24**).

Any visible lesion(s)?

1. Yes

2. No

**Figure 24** - First question of the assessment form about metastatic lesion detection.

The second inquiry was related to the considered image quality on a five-point numerical scale (having “poor”, “medium” and “good” as a reference). The third question was thought to evaluate the diagnostic acceptability (“fully acceptable”, “probably acceptable”, “only acceptable under limited conditions” and “unacceptable”) (**Figure 25**).

	Poor	Medium		Good	
<b>Image Quality</b>	1	2	3	4	5
	<input type="radio"/>	<input type="radio"/>	<input type="radio"/>	<input type="radio"/>	<input type="radio"/>
<b>Diagnostic Acceptability</b>					
	1. Fully acceptable <input type="radio"/>				
	2. Probably acceptable <input type="radio"/>				
	3. Only acceptable under limited conditions <input type="radio"/>				
	4. Unacceptable <input type="radio"/>				

**Figure 25** - Second and third questions of the assessment form about the image quality and diagnostic acceptability, respectively.

Finally, the closing topic was meant to analyse the lesion location defined by each observer using a human skeleton diagram (**Figure 26**) as it appears in the scintigraphic planar images in order to identify: isolated metastatic lesions, areas of multiple metastatic lesions and lesions with dubitative nature. Furthermore, those lesions described were differentiated by their anatomic region (**Appendix V**).

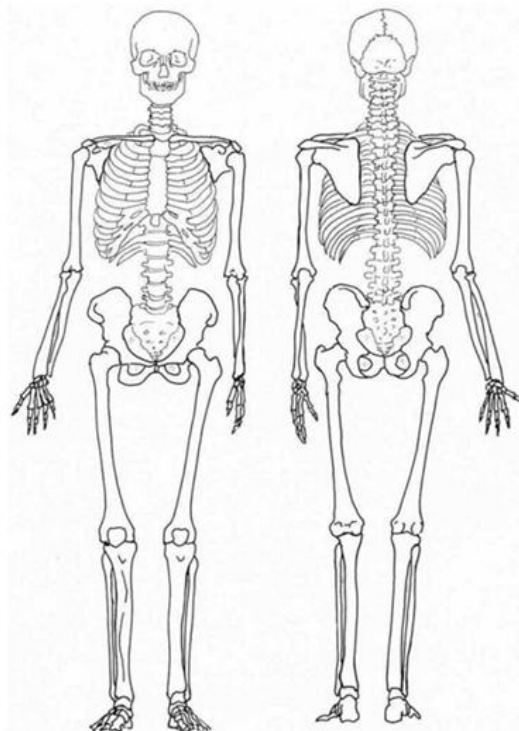


**Figure 26** - Human skeleton diagram of the assessment form using to mark the anatomical location of metastatic bone disease.

Additionally, there was a space for additional comments in which the physicians could describe further relevant information, such as, the presence of suspected lesions. Moreover, it was provided a document with all the necessary instructions for the assessment in order to ensure an equivalent evaluation by all observers (**Appendix VI**).

### 7.3.2. Objective Analysis

The number of counts in a certain area in the images is calculated for a region of interest (ROI) defined by the user. The sum of the counts is assumed to be a proportional measure of a clinically relevant factor.

Two circular ROIs (regions of interest) with same diameter (2.5 cm) were draw on the scans (**Figure 27**) acquired with standard, half-time protocol and processed using EPP software. The selected regions for the ROIs drawing were the medium third of the femur and the soft tissue in the inner thigh (**Appendix VII**). The regions were preferentially set on the right side, unless a bone lesion was present. In those cases, the analysis was performed in the opposite side. However, a patient with bilateral lesions was found so that patient was excluded from this evaluation.

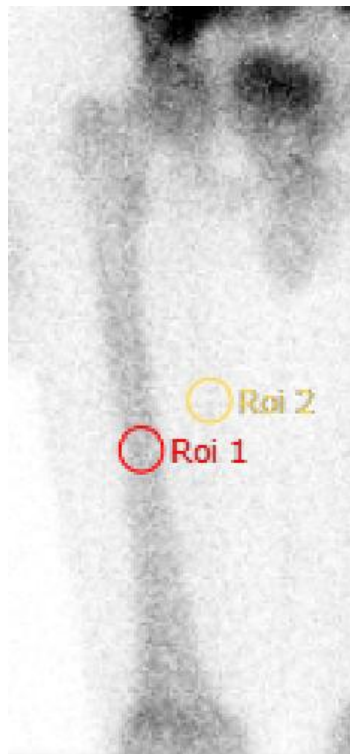


**Figure 27** - The two circular ROIs set in the medium third of the femur and in the soft tissue surrounding (inner thigh).

Therefore, for this assessment were selected 150 images from 50 patients, with the intention of obtaining the SNR, CNR and the COV. These ratios were calculated using the following equations (20):

$$\text{SNR} = \frac{\text{Mean (Bone)}}{\text{Standard Deviation (Soft Tissue)}} \quad (5)$$

$$\text{CNR} = \frac{\text{Mean (Bone)} - \text{Mean (Soft Tissue)}}{\text{Standard Deviation (Soft Tissue)}} \quad (6)$$

$$\text{COV} = \frac{\text{Standard Deviation (Bone)}}{\text{Mean (Bone)}} \quad (7)$$

#### 7.4. Statistical Analysis

Collected data was analysed in terms of absolute and relative frequencies of each variable studied (descriptive statistics) using Statistical Package for the Social Sciences (SPSS) version 20.

The difference in detection accuracy of the three imaging modalities was compared using the one-way ANOVA statistical test. The  $p$ -value of  $\leq 0.05$  was considered as statistically significant, and the 95% confidence interval for such results was calculated. Moreover, it is important to mention that the sample has a normal distribution and for this reason parametric tests were used.

The full-count images were used as the reference standard, and both half-count and EPP-processed images were assessed against this, using interobserver agreement as the measure of quality.

These full-count versus half-count and EPP processed interobserver agreement levels were calculated as fractions and  $k$  values. Interobserver agreement can be measured in any situation in which two or more independent observers are evaluating the same thing. On the other hand, intraobserver agreement should be applied when the same observer evaluate the same thing at two different moments. Therefore, in this particular study, only the interobserver agreement was measured.

## 8. Results

### 8.1. Sample Characterization

As mentioned above, a total sample of 51 patients was randomly recruited to be part of this study. The patients included were directed to the Nuclear Medicine department for bone scintigraphy for suspected metastatic bone disease. Of these, 41 were referred with prostate carcinoma and 10 with breast cancer. No additional criteria were used to select the patients. The patient's average age was 68 years old (ranging between 42-89).

### 8.2. Subjective Assessment

The results obtained through the subjective assessment are described in the following topics.

#### 8.2.1. Metastatic Lesion Detection

The first physician (observer A) diagnosed 35 full-count scans as representing metastatic bone disease compared with 34 half-count scans and 35 Pixon-processed scans. The corresponding figures for observer B were 34, 33 and 32, respectively. On the other hand, observer C diagnosed 35 full-count scans as metastatic bone disease and 37 half-count and Pixon-processed scans as having metastases (**Table 2**).

**Table 2** – Number of scans diagnosed with metastatic bone disease for each image modality by each observer.

	Full-count (n=51)	Half-count (n=51)	Pixon-Processed (n=51)
<b>Observer A</b>	35	34	35
<b>Observer B</b>	34	33	32
<b>Observer C</b>	35	37	37

In this case, no significant differences were found between the different image modalities ( $p > 0.05$ ). The 3 observers made the same diagnosis when viewing a patient's full-count scan as when viewing his/her half-count scan in 47 of the 51 cases (93% or  $k = 0.85$ ). On the other hand, they made the same diagnosis in 49 of the 51 cases, when viewing a patient's full-count scan as when viewing the corresponding EPP-processed scan (95% or  $k = 0.88$ ).

### 8.2.2. Image Quality

The second outcome of the study was to score the image quality of the three different image types. Of the 51 full-count scans evaluated by observer A, 1 was rated as “Poor”, 5 as “Poor/Medium”, 27 as “Medium”, 13 as “Medium/Good” and 5 as “Good”. This was compared with 4, 13, 23, 11 and zero, respectively, for the half-count scans viewed by him/her. Besides, this observer scored 12 EPP-processed scans as “Poor/Medium”, 24 as “Medium”, 11 as “Medium/Good” and 4 as “Good”. For observer B, 2 of the 51 full-count scans were rated as “Poor/Medium”, 14 as “Medium”, 23 as “Medium/Good” and 12 as “Good”. The corresponding values for the half-count scans were 11, 26, 12 and 2, respectively. On the other hand, this observer considered 3 of the 51 EPP-processed scans as “Poor/Medium”, 20 as “Medium”, 24 as “Medium/Good” and 4 as “Good”. In addition, observer C rated 2 full-count scans as “Medium”, 38 as “Medium/good” and 11 as “Good”. Moreover, he/she scored 11 of the 51 half-count scans as “Poor/Medium”, 26 as “Medium”, 12 as “Medium/Good” and 1 as “Good”. The corresponding values for the EPP-processed scans were 16, 30 and 5, respectively (**Table 3**).

**Table 3** – Number of cases scored using the five-point ordinal scale according to the scoring form for the image quality and the mean value achieved by each observer and by each image type.

	Full-count (n=51)	Half-count (n=51)	EPP-Processed (n=51)	Mean Value (Total) (1-5)
<b>Observer A</b>				3.08
1 - “Poor”	1	4	0	
2 - “Poor/Medium”	5	13	12	
3 - “Medium”	27	23	24	
4 - “Medium/Good”	13	11	11	
5 - “Good”	5	0	4	
<b>Mean Value (1-5)</b>	3.31	2.80	3.13	
<b>Observer B</b>				3.52
1 - “Poor”	0	0	0	
2 - “Poor/Medium”	2	11	3	
3 - “Medium”	14	26	20	
4 - “Medium/Good”	23	12	24	
5 - “Good”	12	2	4	
<b>Mean Value (1-5)</b>	3.88	3.10	3.57	
<b>Observer C</b>				3.79
1 - “Poor”	0	0	0	
2 - “Poor/Medium”	0	11	0	
3 - “Medium”	2	26	16	
4 - “Medium/Good”	38	12	30	
5 - “Good”	11	1	5	
<b>Mean Value (1-5)</b>	4.17	3.41	3.78	
<b>Mean Value (Total) (1-5)</b>	3.79	3.10	3.50	



The combined subjective levels of image quality are shown in **Figure 28**. In the highest image quality category (“Good”), the largest number of images was full-count scans, followed by EPP-Processed scans and then half-time scans. At the other extreme, in the “Poor” category the largest number of images was half-time scan, followed by full-count scans. In this category, no EPP-Processed scans were scored as having “Poor” image quality.

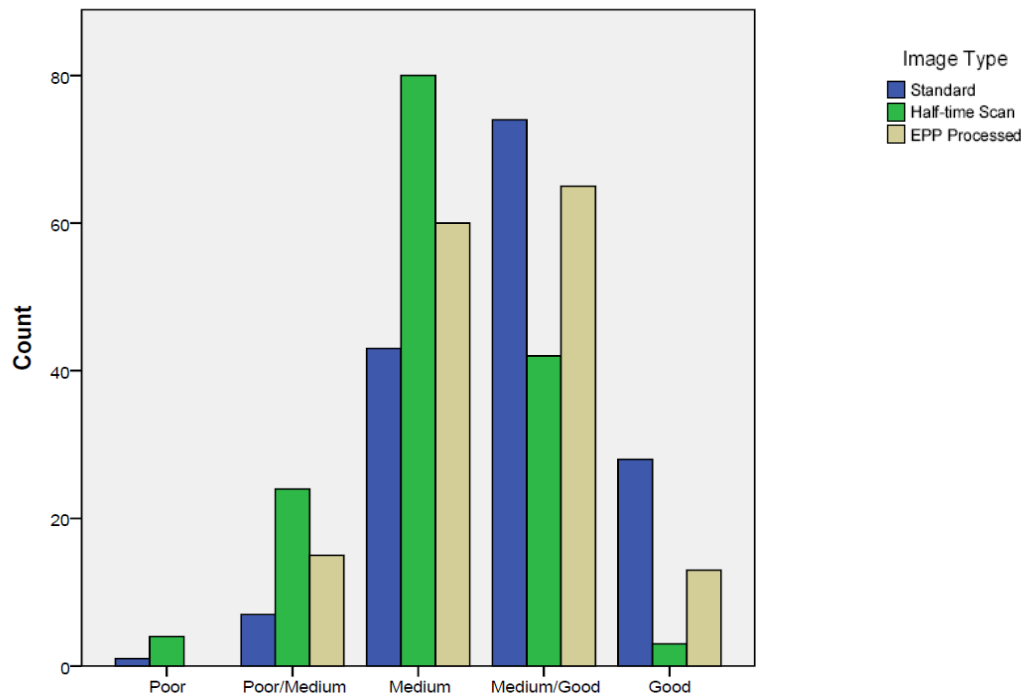


**Figure 28** - Combined image quality scores of the three observers by image type.

In this case, since significant differences were found ( $p \leq 0.05$ ), the interobserver agreement was not calculated. Despite this, it is important to mention that the total mean values for the image quality of the three image modalities are very close from each other (full-count=3.79; half-count=3.10; EPP-Processed=3.50).

### 8.2.3. Diagnostic Acceptability

The third inquiry of the assessment form was about diagnostic acceptability. Thus, observer A scored 15 of the 51 full-count scans as “Fully Acceptable”, 26 as “Probably Acceptable”, 9 as “Only Acceptable Under Limited Conditions” and 1 as “Unacceptable”. The same observer rated 6 half-count scans as being “Fully Acceptable”, 22 as “Probably Acceptable”, 17 as “Only Acceptable Under Limited Conditions” and 6 as “Unacceptable”. Besides, this observer considered 12 of the 51 EPP-Processed scans as “Fully Acceptable”, 21 as “Probably

Acceptable”, 18 as “Only Acceptable Under Limited Conditions”, and for him/her there were no scans “Unacceptable” in terms of diagnostic acceptability.

On the other hand, of the 51 full-count scans viewed by observer B, 36 were rated as “Fully Acceptable”, 12 as “Probably Acceptable”, 2 “Only Acceptable Under Limited Conditions” and 1 as “Unacceptable”. The corresponding values of half-count scans were 20, 21, 9 and 1, respectively. Finally, according to his/her opinion, 32 EPP-processed scans were scored as “Fully Acceptable”, 17 as “Probably Acceptable”, 1 as “Only Acceptable Under Limited Conditions” and 1 as “Unacceptable”. For observer C, 48 full-count scans were considered as “Fully Acceptable” and 3 as “Probably Acceptable”. In addition, of the 51 half-count scans, 32 were scored as “Fully Acceptable”, 18 as “Probably Acceptable” and 1 as “Only Acceptable Under Limited Conditions”. The corresponding values of EPP-processed scans were 43, 7 and 1, respectively (**Table 4**).

**Table 4** - Number of cases scored using o the four-point ordinal scale according to the scoring form for the diagnostic acceptability and the mean value achieved by each observer and by each image type.

	Full-count (n=51)	Half-count (n=51)	EPP-Processed (n=51)	Mean Value (Total) (1-4)
<b>Observer A</b>				2.18
1 - “Fully Acceptable”	15	6	12	
2 - “Probably Acceptable”	26	22	21	
3 - “Only Acceptable Under Limited Conditions”	9	17	18	
4 - “Unacceptable”	1	6	0	
<b>Mean Value (1-4)</b>	1.92	2.45	2.11	
<b>Observer B</b>				1.54
1 - “Fully Acceptable”	36	20	32	
2 - “Probably Acceptable”	12	21	17	
3 - “Only Acceptable Under Limited Conditions”	2	9	1	
4 - “Unacceptable”	1	1	1	
<b>Mean Value (1-4)</b>	1.38	1.82	1.43	
<b>Observer C</b>				1.20
1 - “Fully Acceptable”	48	32	43	
2 - “Probably Acceptable”	3	18	7	
3 - “Only Acceptable Under Limited Conditions”	0	1	1	
4 - “Unacceptable”	0	0	0	
<b>Mean Value (1-4)</b>	1.06	1.39	1.18	
<b>Mean Value (Total) (1-4)</b>	1.45	1.89	1.58	

In the highest image quality category (“Fully Acceptable”), the largest number of images was full-count scans, followed by EPP-Processed scans and then half-time scans. On the other hand, in the “Unacceptable” category the largest number of images was half-time scan, followed by EPP-Processed scans and then full-count scans (**Figure 29**).

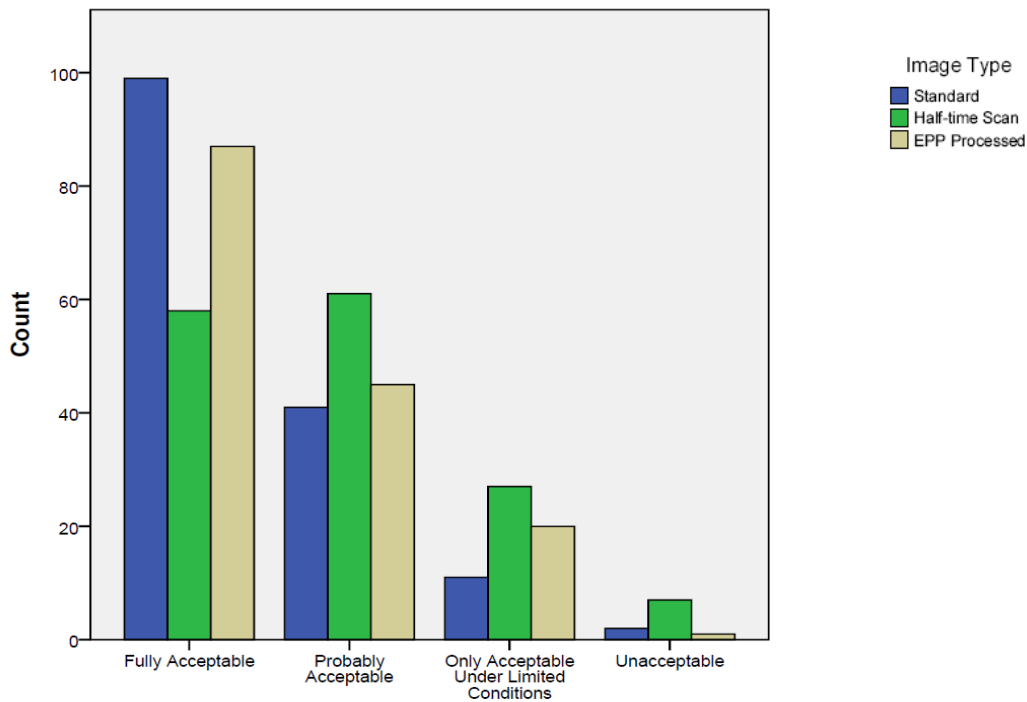


**Figure 29** - Combined diagnostic acceptability scores of the three observers by image type.

In terms of diagnostic acceptability, significant differences were found comparing full-count scans with the half-count scans ( $p \leq 0.05$ ). On contrary, comparing full-count scans with EPP-processed scans, no differences were found ( $p > 0.05$ ). Therefore, the interobserver agreement was measured between these image types and the 3 observers made the same diagnosis when viewing a patient’s full-count scan as when viewing his or her EPP-Processed scan in 36 of the 51 cases (70.6% or  $k=0.48$ ). Despite this, it is important to mention the mean values for full-count, half-count and EPP-Processed scans, were 1.45, 1.89, 1.58, respectively (**Table 4**).

### 8.2.4. Anatomical Location

The whole-body distribution of metastatic bone lesions was measured through the human skeleton diagram presented on the assessment form, in which the physicians were asked to mark the anatomical areas of visualizations of the metastatic lesions.

As expected, in patients referred for suspected metastatic bone disease from prostate cancer, the pelvis was one of the most affected anatomical regions (18.5%). In addition, 18.5% of the lesions were also found in the chest. Lumbosacral spine and the upper limb were the second site more affected by metastases (14.6%), following by dorsal spine (13.8%), head (10%), cervical spine (5.4%) and lower limb (4.6%). On the other hand, in patients with breast cancer, chest was the most affected anatomical area (28.7%), as expected. The lumbar spine, pelvis and hips and lower limb were affected in 14.3% of the cases and these patients had metastatic bone lesions in head, cervical spine, dorsal spine and upper limb in 7.1% of the cases (**Figure 30**).

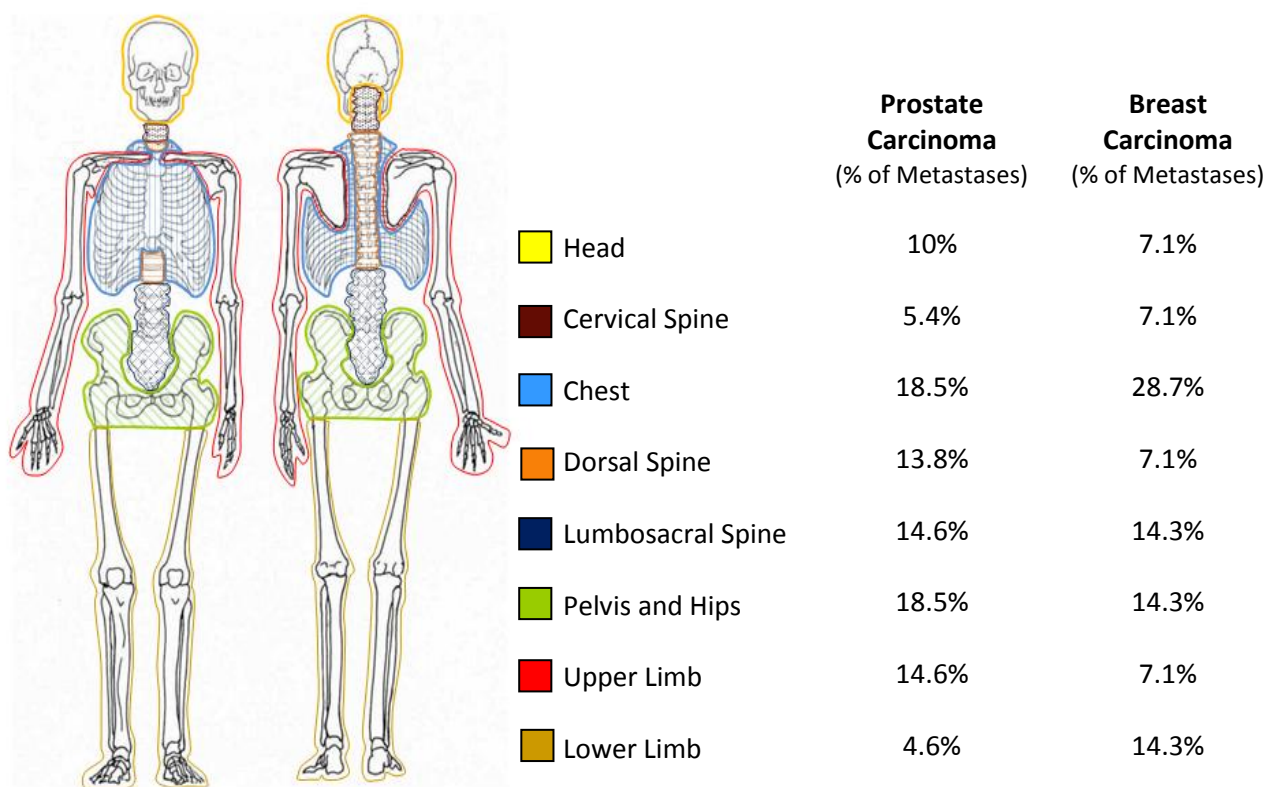


**Figure 30** - Frequency of bone metastases in patients with prostate and breast cancer and the respective anatomical location, according to the human skeleton diagram presented on the assessment form.

In patients with prostate carcinoma, as expected, lumbosacral spine and pelvis were two of the most affected regions. Since no significant differences were found ( $p>0.05$ ), the interobserver agreement between full-count and half-count scans ( $k=0.83$ ) and between full-count and EPP-Processed scans ( $k=0.91$ ) was measured for these particularly cases.

However, as mentioned above, in breast carcinoma patients, the most affected region by bone metastases was the chest. Since the  $p$ -value was not significant ( $p>0.05$ ), the interobserver agreement was calculated between full and half-count scans ( $k=0.87$ ) and between full and EPP-Processed scans ( $k=0.87$ ), for this anatomical region (**Table 5**).

**Table 5** – Interobserver agreement rates in diagnosis of bone metastases using half-count or EPP-Processed scans compared with full-count scans in the most affected anatomical regions by each type of carcinoma.

	FC vs. HC	FC vs. EPP
<b>Prostate Carcinoma</b>		
Pelvis and Hips <b>k-value</b>	0.82	0.97
Lumbosacral Spine <b>k-value</b>	0.83	0.92
<b>Breast Carcinoma</b>		
Chest <b>k-value</b>	0.84	0.84

### 8.2.5. Diagnostic Confidence

The secondary outcome of this study was to measure the confidence each physician felt in making diagnoses according to the scanning modality they were viewing, based on the additional comments in the assessment form (certain of the diagnosis/suspected metastatic lesions). Thus, observer A had certain of the diagnosis in 44 of the 51 total full-scans and had no certain in 6 of these scans. However, this observer mentioned that in 1 full-count scan some lesions were from metastatic disease and others could be metastases or from other nature. According to observer B, 45 of the 51 full-count scans were scored as confident and 4 scans had some lesions from dubitative nature. Besides, in 2 of the 51 full-count scans

he/she observed metastatic lesions and other suspected lesions. The equivalent values for observer C were 39, 5 and 7.

Regarding to EPP-Processed scans, for observer A, 44 presented a confident diagnosis, 6 presented some suspected lesions, hindering the diagnostic proposes and 1 of these scans had metastatic lesions and suspected lesions as well. In opposite, observer B considered 48 scans as having confident diagnosis, 2 as having not confident diagnosis and 1 as having fairly confidence. The corresponding figures for observer C were 35, 6 and 10 (**Table 6**).

**Table 6** – Confidence of physicians in deciding whether an image represents metastatic bone disease: number of cases/scans by each image type.

	Full-count (n=51)	Half-count (n=51)	EPP-Processed (n=51)
<b>Observer A</b>			
“Certain”	44	43	44
“Suspected”	6	6	6
“Certain and Suspected”	1	2	1
<b>Observer B</b>			
“Certain”	45	49	48
“Suspected”	4	1	2
“Certain and Suspected”	2	1	1
<b>Observer C</b>			
“Certain”	39	37	35
“Suspected”	5	5	6
“Certain and Suspected”	7	9	10

The existence of statistical differences was calculated, with a  $p>0.05$  meaning that no significant differences were found. Therefore, the interobserver agreement between the different image modalities was measured. Observer A, B and C came to the same diagnosis when viewing a patient’s full-count scans as when viewing the corresponding half-count scans in 44 of the 51 cases (86.93% or  $k=0.54$ ). On the other hand, they came to the same diagnosis when viewing a patient’s full-count and the EPP-Processed scans in 46 cases (90.2% or  $k=0.66$ ).

### 8.3. Objective Assessment

The results related to the objective assessment are presented and described in the following topic.

#### 8.3.1. SNR, CNR and COV

Concerning the objective assessment, the mean value of the SNR for full-count scans was 8.19 and the standard deviation was 2.29. Concerning the half-count scans, the mean value found was 5.79 and with a standard deviation of 1.68. On the other hand, the standard deviation of the EPP-Processed scans was 2.26 and the mean of 8.10.

Regarding the CNR, it is possible to observe a mean value of 5.59, 4.06 and 5.60 for the full-count, half-count and EPP-Processed scans, respectively.

The last parameter calculated through the objective evaluation was the coefficient of variation. The mean value found for the full-count scan was 0.32 and the corresponding value for the half-count scans was 0.47. On the other hand, for the EPP-Processed scans, the mean value was 0.33 (**Table 7**).

It is important to mention the presence of significant differences ( $p \leq 0.05$ ) comparing half-count scans with full-count and EPP-Processed Scans in terms of SNR, CNR and COV. In contrary, between full-count and EPP-Processed scans no significant differences were found ( $p > 0.05$ ).

**Table 7** – Mean  $\pm$  standard deviation of SNR, CNR and COV for each image type.

	SNR	CNR	COV
	$\bar{X} (\pm SD)$	$\bar{X} (\pm SD)$	$\bar{X} (\pm SD)$
<b>Full-count</b>	8.19( $\pm 2.29$ )	5.59( $\pm 2.35$ )	0.32( $\pm 0.10$ )
<b>Half-count</b>	5.79( $\pm 1.68$ )*	4.06( $\pm 1.74$ )*	0.47( $\pm 0.16$ )*
<b>EPP-Processed</b>	8.10( $\pm 2.26$ )	5.60( $\pm 2.35$ )	0.33( $\pm 0.11$ )
* $p \leq 0.05$			

## **9. Discussion**

The implementation of the EPP software in clinical practice has been studied by many authors and institutions. Most of these studies were performed for bone scintigraphy using a sample of adult patients, but some of them were executed for others Nuclear Medicine procedures, as for example, the dynamic renal scintigraphy in paediatric patients (55-58). Moreover, other authors investigated the performance of Pixon method for different radiopharmaceuticals in order to provide a broad range of patient scintigraphic data for testing (50). The equipment used in the previous studies were different from each other but, despite the fact that Pixon is marketed by Siemens Medical Solutions, it was not developed for a specific camera or manufacturer and, unlike resolution recovery software, does not require knowledge of gamma camera parameters (56).

The Pixon method is designed to manipulate the half-count images to make them appear equal in counts to a full-count image. The half-count images are the result of acquired time reduction or noise addition by specific software. Thus, the half-count images have higher levels of SNR and CNR when processed by EPP software (57).

The main point of this investigation was to understand whether switching from full-count scanning to half-count scanning would introduce significant errors when diagnosing metastatic bone disease and if applied EPP software these errors were reduced. Since the objective was to implement this software at the department of Radiology and Nuclear Medicine at the Radboud University Medical Centre, all the gamma cameras available were used to data collection (Symbia S and Symbia T16 dual head gamma cameras). The images were acquired using the department's standard protocol with a scan speed of 8 cm/min and then with 16 cm/min. The images acquired with the shorter acquisition time were processed using the EPP software based on Pixon method, previously described. In this particular study, two different types of evaluation were performed: a subjective and an objective assessment (38,58).

### **9.1. Subjective Assessment**

The subjective assessment is probably the most common method of image evaluation when it comes to diagnostic imaging (50,56,57,58). According to this, it is important to anonymize all the images in order to not influence the physician's opinion. The results related to the subjective assessment were achieved after a triple "blind" evaluation performed by three Nuclear Medicine physicians according to a provided scoring form. The physicians were asked to score all the images in terms of metastatic lesion detection, image quality, diagnostic acceptability, metastatic lesion location and diagnostic confidence.



### 9.1.1. Metastatic Lesion Detection

The levels of agreement between the diagnoses of metastatic bone disease enable us to address the main question of this investigation: would switching from full-count scanning to half-count scanning introduce significant errors when diagnosing metastatic bone disease and would Pixon processing reduce these errors? It represents how often all physicians arrive at the same diagnosis, viewing different image modalities. However, this effect was not statistically significant ( $p>0.05$ ) as demonstrated before by other authors (56,58).

Hence, the three physicians viewing full-count scans and the corresponding half-count scans agreed in 93% of cases (or  $k=0.85$ ), similarly when they were viewing full-count scans and corresponding EPP-Processed scans (they agree in 95% of scans or  $k=0.88$ ). Therefore, it is possible to conclude that there was an almost perfect agreement between physicians when they were presented with the half-count and EPP-Processed scans against corresponding full-count scans (those were used as the standard reference).

As a result, the half-count scans suggested a little improvement in diagnostic accuracy when including the Pixon-processing step. This condition probably happens due to the noise improvement (and relative contrast), the processed images show some specific structures much better than conventional images. These structures include ribs, pelvis and long bones (50).

### 9.1.2. Image Quality

With the respect to the second outcome of this study, the image quality of the scans, significant differences between the three image modalities ( $p\leq 0.05$ ) were found. Thus, the observers considered the images acquired with the full-count protocol, the images with best image quality, following by EPP-Processed scans and for half-count scans. However, this result could be influenced by the physician's experience since less experienced physicians are more exigent in terms of scan's image quality.

Despite the fact that significant differences were found, it is important to mention that the mean values for the three images type, according to the five-point ordinal scale presented on the assessment form (where 1 means "Poor" and 5 means "Good") were very close from each other (full-count=3.79; half-count=3.10; EPP-Processed=3.50).

In the highest category of quality ("Good"), the largest number of images was full-count scans, followed by EPP-Processed images and then half-count scans. At the other extreme, in "Poor" category the largest number of images was half-count scans, followed by full-count images. In this case, no images acquired with the half-time protocol and processed with the EPP software were considered as "Poor" in terms of image quality. In other words, physicians prefer the quality of the full-count scans, but the image quality of the EPP-

Processed scans is completely acceptable for diagnostic proposes, as already demonstrated (57).

### 9.1.3. Diagnostic Acceptability

Regarding the third inquiry of this investigation, the diagnostic acceptability, it is possible to see the presence of significant differences between full-count and half-count scans ( $p \leq 0.05$ ). On the other hand, no significant differences were found between the images acquired with the full-count protocol and the ones acquired with the half-count protocol and processed with EPP software ( $p > 0.05$ ). Moreover, for this particularly case, there was a moderate agreement ( $k = 0.48$ ) between observers. In the maximum diagnostic acceptability category ("Fully Acceptable") the largest number of images were full-count scans, followed by EPP-Processed scans and then half-count scans. On the other hand, in "Unacceptable" category the largest number of images was half-count scans, followed by full-count scans and then EPP-Processed scans. Therefore, it is easy to understand that the EPP-processed scans have an equivalent diagnostic acceptability of the scans acquired with the standard protocol, entirely acceptable for diagnostic proposes.

### 9.1.4. Lesion Location

In this investigation, it was also calculated which were the anatomical regions more affected by metastatic bone disease. In patients with prostate carcinoma, the pelvis (18.5% of cases) and the lumbar spine (14.6% of cases) were two of those areas. These two areas are frequently affected in this kind of disease, being the first area for which the physicians look when they are presented with whole-body bone scans (59). For that reason, the interobserver agreement was measured in these areas, translating into an almost perfect agreement when comparing the full-count with half-count scans ( $k = 0.83$ ) and with EPP-Processed scans ( $k = 0.91$ ), with no significant differences ( $p > 0.05$ ).

On the other hand, in breast carcinoma patients, the most affected region was the chest (28.7% of cases), as referred in the first chapter of this document (60). Moreover, there was an almost perfect agreement ( $k = 0.87$ ) between observers when viewing half-count or EPP-Processed scans compared with full-count scans.

Since no significant differences were found in terms of lesion detection in the most affected anatomical regions by metastatic bone disease, the first outcome of this investigation is validated. Therefore, the images acquired with the half-time protocol and processed with the EPP software were considered with sufficient diagnostic accuracy in order to detect the presence or not of metastases. As mentioned above, the processed images show some specific structures much better than conventional images, including ribs and pelvis (50).

### 9.1.5. Diagnostic Confidence

In what concerns the secondary outcome measure, the subjective confidence of physicians in the diagnoses they are making, it became possible to see that no significant differences were found ( $p>0.05$ ) comparing the full-count scans with the half-time and the EPP-Processed scans. Besides, the interobserver agreement between the images acquired with the full-count and half-count protocol was moderate ( $k=0.54$ ) and between full-count and EPP-Processed scans was considered as substantial ( $k=0.66$ ). Thus, it is possible to recognize that physicians felt confident in making diagnoses using any image modality. Actually, the full-count scans may be aesthetically more pleasing, resulting in great physician confidence, but in fact may not represent any true ability to make more accurate diagnoses, as demonstrated before by other studies (56).

## 9.2. Objective Assessment

The objective assessment results were achieved through the calculation of SNR, CNR and COV. These values were calculated setting two circular ROIs in the prints generated to the subjective assessment purpose. One of the circular ROI was draw in the third medium of the femur and the other one in the inner thigh.

### 9.2.1. SNR, CNR and COV

Concerning the objective analysis, the best signal-to-noise ratio was found in images acquired with the full-count protocol (mean=8.19), followed by EPP-processed (mean=8.10) scans and then the half-count scans (mean=5.79). In terms of contrast-to-noise ratio, the highest and consequently the best value was found in the scans acquired with the half-time protocol and processed with the EPP software (mean=5.60), followed by images acquired with full-count protocol (mean=5.59) and by half-count scans (mean=4.06). With respect to the last parameter measured through the objective assessment, the coefficient of variation, it is possible to conclude that the lowest value was obtained in full-count scans (mean=0.32) and the highest value was obtained using the half-count scans (mean=0.47). The mean value of coefficient of variation for scans processed using the EPP software was 0.33.

However, it was found significant differences in full-count compared with half-time scans ( $p\leq 0.05$ ) and between full-count and EPP-Processed scans the differences were not significant ( $p>0.05$ ). In other others, the images acquired with the half-time protocol have higher levels of noise because of the reduction of the acquisition time and consequently the reduction of the number of counts. The EPP software, based on Pixon method improved those levels making the image more homogenous and more acceptable in terms of signal and contrast, increasing the levels of SNR and CRN (58).

### **9.3. Limitations**

There are two basic methods for characterizing image quality: physical characteristics such as spatial resolution, contrast and noise, which can be quantitatively measured or calculated; and qualitative methods, such as human observation. The images obtained during this study were evaluated by means of human observer performance. Due to the complexity of the human vision and other influencing factors like observer experience, this method can be uncertain in terms of its objectivity. However, in most cases, object detectability is determined more accurately by direct evaluation using human observers (61). On the other hand, since the images were evaluated only once by each physician it was not possible to measure the intraobserver agreement between the same image modality (62).

Finally, the reconstruction parameters of the EPP software are automatic, and impossible to change. It is also possible that different Pixon settings would be appropriate depending on the camera or scanning technique used. The sensitivity and the resolution of the cameras used in this investigation were very similar, and there were no discernible differences in image quality between the different models. Although, as mentioned above, EPP is marketed by Siemens Medical Solutions and it was not developed for a specific camera or even manufacturer. It therefore seems unlikely for different cameras or that the effect of the software would be changed with standard scanning conditions, but this effect was not tested in this study (56). These points could be investigated in the future, as well as the reduction of acquisition time, as much as possible. In this particular case, for future investigations these limitations can be analysed and it would also be important to investigate if the time could be reduced for less than half, taking in consideration that in this project was only investigated the time reduction to half.

However, and despite the fact of the existence of some limitations, the EPP software is currently used in clinical practice and it is considered valid for diagnostic purposes.

## **10. Conclusion**

In the evaluation of oncological patients, bone scan provides the essential information related to the sites of osseous metastases, their prognosis and evaluation of osseous tumour response to chemotherapy and radiation therapy.

In order to generate an adequate diagnostic image in Nuclear Medicine, an appropriate balance between image quality and radiation dose is required. In principle, it would be advantageous to reduce the number of counts collected in bone scanning from a financial and a radiation protection point of view, provided this can be achieved without loss of diagnostic accuracy. On the other hand, images obtained in Nuclear Medicine procedures can have high levels of noise, resulting in interpretation difficulties.

Presently, improvement of image quality is possible through the application of image processing tools. According to this, this study aimed to assess the performance of an EPP algorithm in clinical practice regarding diagnosis and reader confidence, so that the safe employment of the software can be warranted.

With this study results is possible to conclude that halving the number of counts does not introduce significantly disagreement when diagnosing metastatic bone disease. Moreover, the physicians feel confident making diagnosis with any type of image modality, including the images acquired with the half-time protocol and processed with EPP software. For diagnostic proposes they consider the scans acquired with the half-time protocol and processed with EPP software better than the scans acquired using the half-time protocol no processed. This condition is also confirmed with the levels of SNR, CNR and COV measured in this investigation, since the noise is significantly reduced when the software is applied.

At the end of this investigation, it is possible to say that the EPP software improves the image quality of the scans acquired when the acquisition time is reduced in 50%. It was determined that the Pixon method was effective in reducing a patient's bone scan time while achieving comparable quality images. Since the patients submitted to whole-body bone scans can experience pain and anxiety during the examination and even for the department's workflow, the EPP software is a safe and a useful processing technique to implement at the department. Therefore, the utilization of this technology not only has the potential to increase patient satisfaction, but also increase patient throughput in the department.

## Bibliographic References

1. **International Atomic Energy Agency (IAEA).** *Criteria for Palliation of Bone Metastases - Clinical Applications.* ISBN: 92-0-104507-7. 2007.
2. *Tumor metastasis to bone.* **Virk, Mandeep S. and Lieberman, Jay R.** 2007, *Arthritis Research & Therapy*, Vol. 9. DOI: 10.1186/ar2169.  
Available at: <http://www.ncbi.nlm.nih.gov/pmc/articles/PMC1924520/pdf/ar2169.pdf>.
3. *Clinical Features of Metastatic Bone Disease and Risk of Skeletal Morbidity.* **Coleman, Robert E.** s.l. : American Association for Cancer Research, 2006, *Clinical Cancer Research*, Vol. 12. Available at: <http://clincancerres.aacrjournals.org/content/12/20/6243s.full.pdf+html>.
4. *Comparison between solitary and multiple skeletal metastatic lesions of breast cancer patients.* **Koizumi, M., et al.** s.l. : European Society for Medical Oncology, 2003, Vol. 14, pp. 1234-1240. DOI: 10.1093/annonc/mdg348. Available at: <http://annonc.oxfordjournals.org/content/14/8/1234.full.pdf+html>.
5. *Predictors of survival in patients with prostate cancer and spinal metastasis.* **Dan Michael Drzymalski, B. A., et al.** Spine, s.l. : Journal of Neurosurgery, 2010, Vol. 13. DOI: 10.371/2010.6. Available at: <http://ria.ua.pt/bitstream/10773/1980/1/2009000530.pdf>.
6. *Pathophysiology of Bone Metastases: How This Knowledge May Lead to Therapeutic Intervention.* **Lipton, Allan.** 2004, *The Journal of Supportive Oncology*, Vol. 2, pp. 205-220. Available at: <http://www.oncologypractice.com/jso/journal/articles/0203205.pdf>.
7. **Kini, Usha and Nandeesh, B. N.** *Physiology of Bone Formation, Remodeling, and Metabolism.* [book auth.] Ignac Fogelman, Gopinath Gnanasegaran and Hans Wall. *Radionuclide and Hybrid Bone Imaging.* s.l. : Springer, 2013, pp. 29-55.
8. **Jacofsky, David J., Frassica, Deborah A. and Frassica, Frank J.** *Metastatic Disease to Bone.* *Hospital Physician.* 2004, Vol. 39, pp. 21-28.  
Available at: [http://www.turner-white.com/memberfile.php?PubCode=hp\\_nov04\\_bone.pdf](http://www.turner-white.com/memberfile.php?PubCode=hp_nov04_bone.pdf).
9. **Torbert, Jesse T. and Lackman, Richard D.** *Pathological Fractures.* [book auth.] R. J. Pignolo, M. A. Keenan and N. M. Hebel. *Fractures in the Elderly.* s.l. : Springer, 2011, 2, pp. 43-54. Available at: <http://www.springer.com/medicine/family/book/978-1-60327-466-1>.
10. *Imaging bone metastases in breast cancer: techniques and recommendations for diagnosis.* **Costelloe, Coleen M., et al.** 2009, *The Lancet Oncology*, Vol. 10, pp. 606-614. DOI:10.1016/S1470-2045. Available at: [http://www.thelancet.com/journals/lanonc/article/PIIS1470-2045\(09\)70088-9/fulltext#article\\_upsell](http://www.thelancet.com/journals/lanonc/article/PIIS1470-2045(09)70088-9/fulltext#article_upsell).
11. *Bone Imaging in Metastatic Breast Cancer.* **Hamaoka, Tsuyoshi, et al.** s.l. : American Society of Clinical Oncology, 2004, *Journal of Clinical Oncology*, Vol. 22, pp. 2942-2953. DOI: 10.1016/S1470-2045(09)70088-9. Available at: <http://www.ncbi.nlm.nih.gov/pubmed/15254062>.

12. *Radiological imaging for the diagnosis of bone metastases*. **Rybak, L. D. and Rosenthal, D. I.** 2001, The Quarterly Journal of Nuclear Medicine, Vol. 45, pp. 53-64.  
Available at: <http://www.ncbi.nlm.nih.gov/pubmed/11456376>.
13. *Diagnostic imaging methods in metastatic disease*. **Milosevic, Zorica, Gajic-Dobrosavljevic, Marija and Stevanovic, Jasna.** s.l. : Institute of Oncology Sremska Kamenica, 2006. Vol. 14, pp. 73-74.  
Available at: <http://www.onk.ns.ac.rs/archive/Vol14/PDFVol14/V14s1p73.pdf>.
14. *FDG PET and PET/CT: EANM procedure guidelines for tumor PET imaging: version 1.0*. **Boellaard, Ronald, et al.** s.l. : Springer, 2010, Journal of Nuclear Medicine Molecular Imaging, Vol. 37, pp. 181-200. DOI: 10.1007/s00259-009-1297-4.  
Available at:  
[http://www.ncbi.nlm.nih.gov/pmc/articles/PMC2791475/pdf/259\\_2009\\_Article\\_1297.pdf](http://www.ncbi.nlm.nih.gov/pmc/articles/PMC2791475/pdf/259_2009_Article_1297.pdf).
15. *Detection of Bone Metastases: Assessment of Integrated FDG PET/CT Imaging*. **Taira, Al V., et al.** s.l. : RSNA, 2007, Radiology, Vol. 243, pp. 204-211.  
Available at: <http://pubs.rsna.org/doi/abs/10.1148/radiol.2431052104>.
16. *The Detection of Bone Metastases in Patients with High-risk Prostate Cancer: 99mTc-MDP Planar Bone Scintigraphy, Single- and Multi-Field-of-View SPECT, 18F-Fluoride PET, and 18F-Fluoride PET/CT*. **Even-Sapir, Einat, et al.** 2006, Journal of Nuclear Medicine, Vol. 47, pp. 287-297. Available at: <http://www.ncbi.nlm.nih.gov/pubmed/16455635>.
17. *Basic science: nuclear medicine in skeletal imaging*. **Calleja, Michele, et al.** s.l. : Elsevier, 2005. Vol. 19, pp. 34-39. DOI: 10.1016/j.cuor.2005.01.009.  
Available at: <http://www.sciencedirect.com/science/article/pii/S0268089005000101>.
18. **Lee, Jae Sung.** Basic Nuclear Physics and Instrumentation. [book auth.] Edmund E. Kim, et al. *Handbook of Nuclear Medicine and Molecular Imaging*. s.l. : World Scientific, 2012, 1, pp. 3-19.
19. **Mettler, Fred A. and Guiberteau, Milton J.** *Essentials of Nuclear Medicine Imaging*. 5th. s.l. : Elsevier, 2006. ISBN: 0721602010.
20. **Bushberg, Jerrold T., et al.** *The Essential Physics of Medical Imaging*. 3rd. s.l. : Lippincot Williams & Wilkins, 2012. ISBN: 0-683-30118-7.
21. **Madsen, Mark T.** Nuclear Medicine Imaging Instrumentation. [book auth.] Myer Kutz. *Standard Handbook of Biomedical Engineering and Desing*. s.l. : McGraw-Hill, 2004.
22. **Ziegler, Sibylle I. and Dahlbom, Magnus.** Instrumentation and Data Acquisition. [book auth.] A. L. Baert and K. Sartor. *Diagnostic Nuclear Medicine*. 2nd. s.l. : Springer, 2006, 16, pp. 275-290.
23. **Health Protection Agency for the Administration of Radioactive Substances Advisory Committee.** A Review of the Supply of Molybdenum-99, the Impact of Recent Shortages and the Implications for Nuclear Medicine Services in the UK. 2010.
24. **Maher, Kieran.** *Basic Physics of Nuclear Medicine*. s.l. : Libronomia Company, 2006.
25. **Pedroso de Lima, J. J.** *Nuclear Medicine Physics*. s.l. : Coimbra University Press, 2011. ISBN: 978-1-58488-796-6.

26. **Cherry, Simon R., Sorenson, James A. and Phelps, Michael E.** *Physics in Nuclear Medicine*. 4th. s.l. : Elsevier, 2012. ISBN: 978-1-4160-5198-5.
27. **Christian, Paul E. and Waterstram-Rich, Kristen M.** *Nuclear Medicine and PET/CT*. 6th. s.l. : Elsevier, 2007. ISBN: 9780323043953.
28. **Prekeges, Jennifer.** *Nuclear Medicine Instrumentation*. s.l. : Jones and Bartlett, 2012. ISBN: 978-1-4160-5198-5.
29. **Society of Nuclear Medicine.** *Procedure Guideline for Bone Scintigraphy*. 2003. pp. 205-209. Available at: [http://snmmi.files.cms-plus.com/docs/pg\\_ch34\\_0403.pdf](http://snmmi.files.cms-plus.com/docs/pg_ch34_0403.pdf).
30. *Bone scintigraphy: procedure guidelines for tumour imaging*. **EANM**. 2003, European Journal of Nuclear Medicine Molecular Imaging, Vol. 30. DOI: 10.1007/s00259-003-1347-2. Available at: [http://www.eanm.org/publications/guidelines/gl\\_onco\\_bone.pdf](http://www.eanm.org/publications/guidelines/gl_onco_bone.pdf).
31. Introduction to Medical Imaging. [book auth.] Hodder Arnold. *Imaging for Students*. s.l. : David A Lisle, 2012.
32. **Britton, K. E.** Nuclear Medicine Imaging in Bone Metastases. *Cancer Imaging*. 2002, Vol. 2, pp. 84-86.
33. **Schiepers, Christiaan.** Skeletal Scintigraphy. [book auth.] A. L. Baert and K. Sartor. *Diagnostic Nuclear Medicine*. s.l. : Springer, 2006.
34. *Comparison of Image Enhancement Methods for the Effective Diagnosis in Successive Whole-Body Bone Scans*. **Jeong, Chang Bu, et al.** 2011, Journal of Digital Imaging, Vol. 24, pp. 424-436. Available at: [http://www.ncbi.nlm.nih.gov/pmc/articles/PMC3092044/pdf/10278\\_2010\\_Article\\_9273.pdf](http://www.ncbi.nlm.nih.gov/pmc/articles/PMC3092044/pdf/10278_2010_Article_9273.pdf).
35. *Patterns, Variants, Artifacts, and Pitfalls in Conventional Radionuclide Bone Imaging and SPECT/CT*. **Gnanasegaran, Gopinath, et al.** s.l. : Elsevier, 2009. Seminars in Nuclear Medicine. pp. 380-393. DOI: 10.1053/j.semnuclmed. Available at: <http://www.ncbi.nlm.nih.gov/pubmed/19801218>.
36. **Krom, Aaron J., et al.** Evaluation of Image Enhancement Software as a Method of Performing Half-count Scans. *Nuclear Medicine Communications*. 2012, Vol. 34, pp. 78-85. Available at: <http://www.ncbi.nlm.nih.gov/pubmed/23132292>.
37. **Brenner, Arnold I., et al.** *The Bone Scan*. s.l. : Elsevier, 2012. pp. 11-26, Seminars in Nuclear Medicine. DOI: 10.1053/j.semnuclmed. Available at: <http://www.ncbi.nlm.nih.gov/pubmed/22117809>.
38. *Reduction in Radiation Dose in Mercaptoacetyltriglycerine Renography with Enhanced Planar Processing*. **Hsiao, Edward M., et al.** s.l. : RSNA, 2011, Radiology, Vol. 261, pp. 907-915. DOI: 10.1148/radiol.11110602. Available at: <http://www.ncbi.nlm.nih.gov/pubmed/21900613>.
39. **Lorimer, Lisa, et al.** Improvement in DMSA Imaging Using Adaptive Noise Reduction: an ROC Analysis. *Nuclear Medicine Communications*. 2012. Available at: <http://www.ncbi.nlm.nih.gov/pubmed/22914359>.

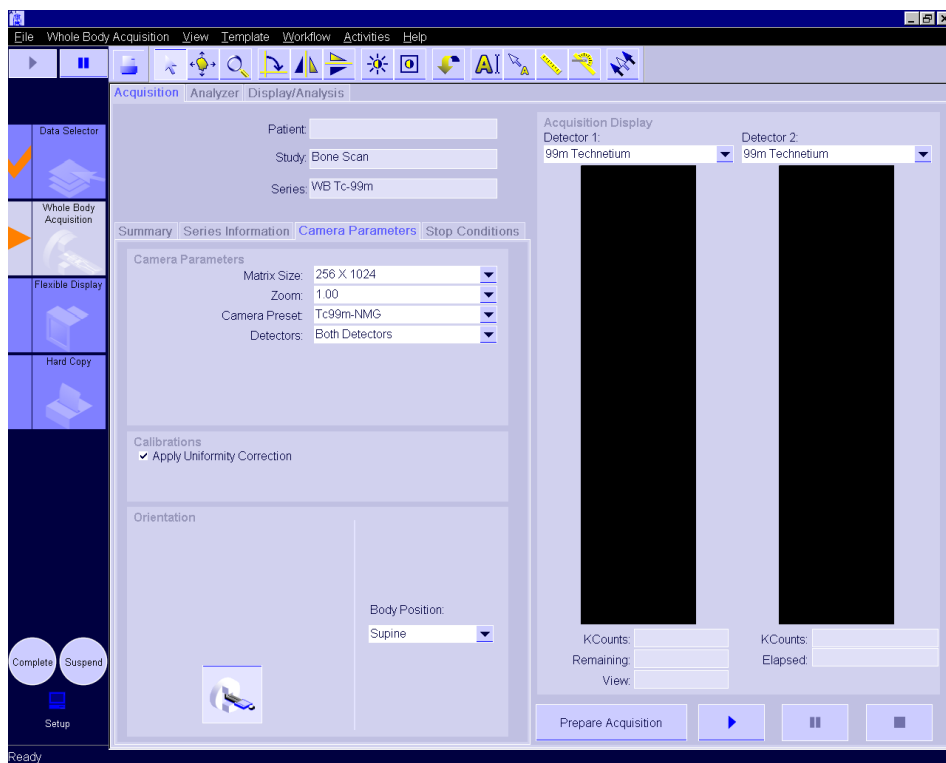


40. **Vija, A. Hans, et al.** *Statistically Based, Spatially Adaptive Noise Reduction of Planar Nuclear Studies*. 2005. DOI: 10.1117/12.595679.  
Available at: <http://spie.org/Publications/Proceedings/Paper/10.1117/12.595679>.
41. **Puetter, R. C., Gosnell, T. R. and Yahil, Amos.** Digital Image Reconstruction: Deblurring and Denoising. *Annual Review of Astronomy and Astrophysics*. 2005, Vol. 43, pp. 139-194. Available at: [http://www.pixon.com/publications/Puetter\\_05\\_ARAA.pdf](http://www.pixon.com/publications/Puetter_05_ARAA.pdf).
42. **Pratt, William K., [ed.].** *Digital Image Processing*. 4th. s.l. : Wiley, 2007. ISBN: 978-0-471-76777-0.
43. *A Review of Image Denoising Algorithms, with a new one.* **Buades, A., Coll, B. and Morel, J. M.** 2005, SIAM Journal on Multiscale Modeling and Simulation 4, Vol. 2, pp. 490-530. DOI: 10.1137/040616024. Available at: <http://ivm.sjtu.edu.cn/files/dip/pro1/NL2.pdf>.
44. **Thie, Joseph A.** *Nuclear Medicine Imaging: An Encyclopedic Dictionary*. s.l. : Springer, 2012. ISBN: 978-3-642-25034-7.
45. **Puetter, Richard C. and Yahil, Amos.** *The Pixon Method of Image Reconstruction*. Cornell University Library. 1999. Available at: <http://cds.cern.ch/record/375890/files/9901063.pdf>.
46. Pixon Applications in Medical Imaging. *Pixon Revealing Reality*. [Online] Pixon, LLC, 2004. [Cited: 26 June 2014.] <http://pixon.com/solutions.html>.
47. The Pixon Method. *Pixon Revealing Reality*. [Online] Pixon LLC, 12 September 2002. [Cited: 28 May 2014.] <http://www.pixon.com/brochure.html>.
48. **Hassanpour, Hamid, Yousefian, Hadi and Zehtabian, Amin.** Pixon-Based Image Segmentation. [ed.] Pei-Gee Ho. *Image Segmentation*. s.l. : InTech, 2011.
49. *A novel pixon-representation for image segmentation based on Markov random field.* **Lin, Lei, et al.** s.l. : Elsevier, 2008, Image and Vision Computing, Vol. 26, pp. 1507-1514. DOI: 10.1007/978-3-642-25035-4. Available at: <http://www.sciencedirect.com/science/article/>.
50. *Improved lesion detection from spatially adaptive, minimally complex, Pixon reconstruction of planar scintigraphic images.* **Wesolowski, Carl A., et al.** s.l. : Elsevier, 2005, Computerized Medical Imaging and Graphics, Vol. 29, pp. 65-81.
51. **Lin, Robert P., Dennis, Brian R. and Benz, Arnold O.** *The Reuven Ramaty High-Energy Solar Spectroscopic Imager - Mission Description and Early Results*. s.l. : Kluwer Academic Publishers, 2003. ISBN: 978-94-017-3452-3.
52. *Pixon-based Miltiresolution Image Reconstruction for Yohkoh's Hard X-ray Telescope.* **Metcalfe, Thomas R., et al.** s.l. : The American Astronomical Society, 1996, The Astrophysical Journal, Vol. 466, pp. 585-594. DOI: 10.1007/978-94-011-5430-7\_45. Available at: <http://link.springer.com/chapter>.
53. *The Information Content of Redshift and Velocity Surveys.* **Yahil, A.** New York : s.n., 1995. XXXth Moriond Meeting "Clustering in the Universe".  
Available at: [http://www.pixon.com/publications/Yahil\\_96\\_Moriond.pdf](http://www.pixon.com/publications/Yahil_96_Moriond.pdf).

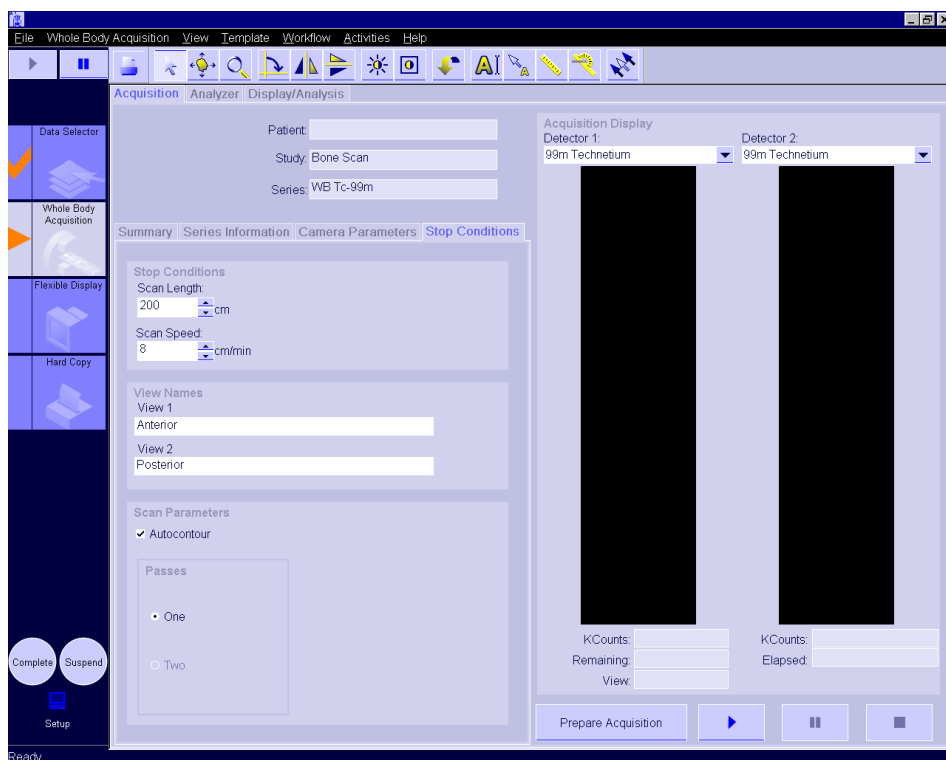
54. RESSI - Reuven Ramaty High Energy Solar Spectroscopic Imager. *HESSI Pixon Tutorial*. [Online] NASA, 16 March 2004. [Cited: 26 June 2014.]  
[http://hesperia.gsfc.nasa.gov/rhessidatcenter/imaging/pixon/pixon\\_tutorial.html](http://hesperia.gsfc.nasa.gov/rhessidatcenter/imaging/pixon/pixon_tutorial.html).
55. *Utilization of the Pixon method with whole body bone imaging*. **Venzke, Clarissa, Grancorvitz, Abigail and Johnson, Carlyn**. 2014, The Journal of Nuclear Medicine, Vol. 55. Available at:  
[http://jnumedmtg.snmjournals.org/cgi/content/meeting\\_abstract/55/1\\_MeetingAbstracts/2712](http://jnumedmtg.snmjournals.org/cgi/content/meeting_abstract/55/1_MeetingAbstracts/2712).
56. *Pixon-based noise reduction algorithm for shorter acquisition time in whole body bone scintigraphy*. **Ardenfors, Oscar, et al**. 2014, The Journal of Nuclear Medicine, Vol. 55. Available at:  
[http://jnumedmtg.snmjournals.org/cgi/content/meeting\\_abstract/55/1\\_MeetingAbstracts/2128](http://jnumedmtg.snmjournals.org/cgi/content/meeting_abstract/55/1_MeetingAbstracts/2128).
57. *Intraobserver and Interobserver Variability in Schemes for Estimating Volume of Brain Lesions on MR Images in Multiple Sclerosis*. **Filippi, Massimo, et al**. Brain Lesions, February 1998, American Journal of Neuroradiology, Vol. 19, pp. 239-244.  
Available at: <http://www.ajnr.org/content/19/2/239.full.pdf>.
58. **Motwani, Mukesh C., Gadiya, Mukesh C. and Motwani, Rakhi C**. *Survey of Image Denoising Techniques*. s.l. : Proceedings of GSPx, 2004.
59. *An Intelligent Approach to Image Denoising*. **Saba, Tanzila, Rehman, Amjad and Sulong, Ghazali**. s.l. : JATIT & LLS, 2010, Journal of Theoretical and Applied Information Technology.
60. *Pixon-Based Multiresolution Image Reconstruction and the Quantification of Picture Information Content*. **Puetter, R. C**. 1995, The International Journal of Image Systems and Technology.
61. **Gregory, Phil**. *Bayesian Logical Data Analysis for the Physical Sciences*. Cambridge : Cambridge University Press, 2005.
62. **Espinosa, J M Rodriguez, Herrero, A and Sanchez, F**. *Instrumentation for Large Telescopes*. Cambridge : Cambridge University Press, 1997.
63. **Puetter, Richard and Yahil, Amos**. *Accelerated Signal Encoding and Reconstruction Using Pixon Methods*. US 6,353,688 B1 United States of America, 05 March 2002.

# Appendix I

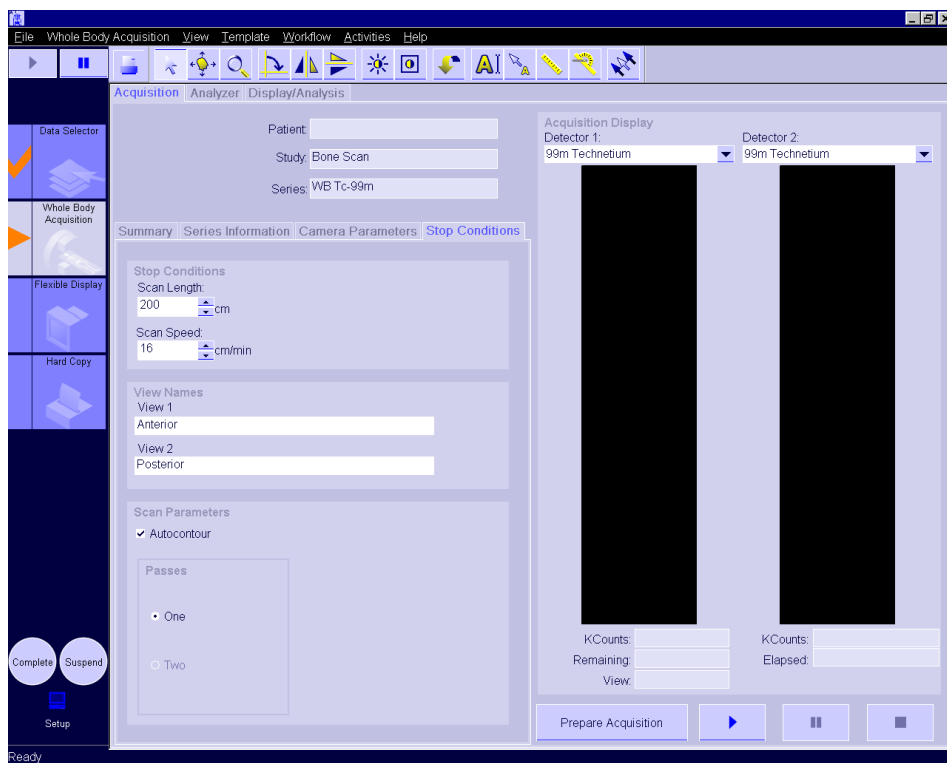
## General Camera Parameters



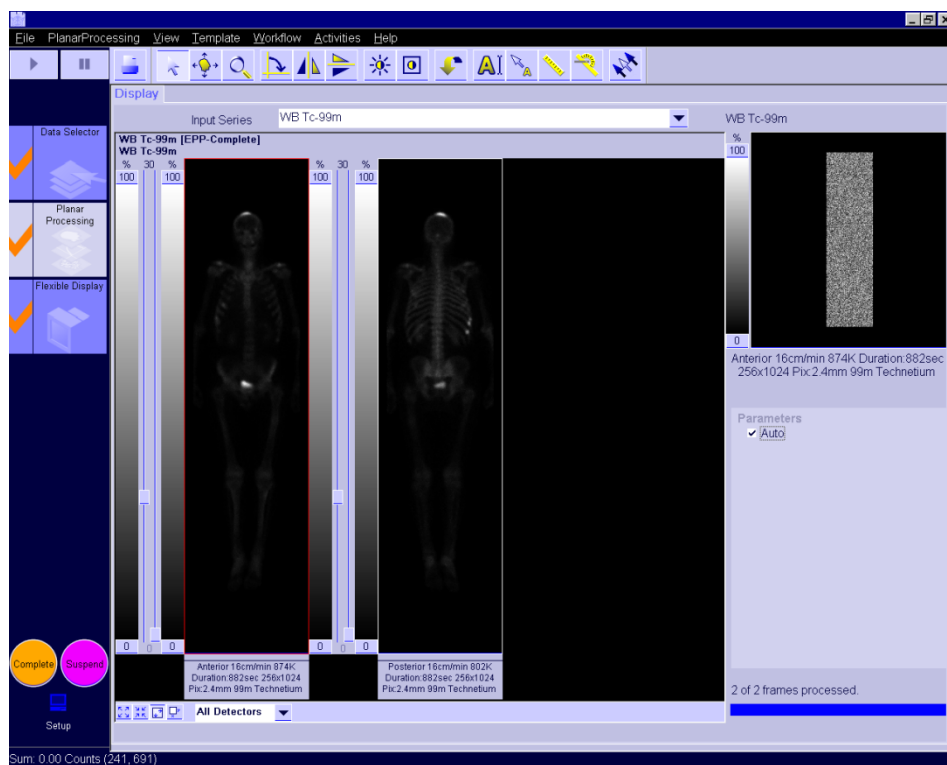
## Stop Conditions for Standard Acquisition



## Stop Conditions for Half-count Acquisition



## Whole-body Enhanced Planar Acquisition Tool



# Appendix II

## Database

HERMES Search: EPP PRINTS

Patient: Patient Name, Patient ID, Gender  
 Study: Description, Study ID, Ref.Phys  
 Series: Description, Body Part, Format  
 Date Restriction: None, Study, Series; Today, Yesterday; Last Week, Last Month, Other

Series Detail: Std Modality, Sub Modality, All, Print, Static, WB, Dyn, Gated, TomoAcq, Trans, Coro, Sagg, GTomoAcq, Text/xml

Sort: Patient Name

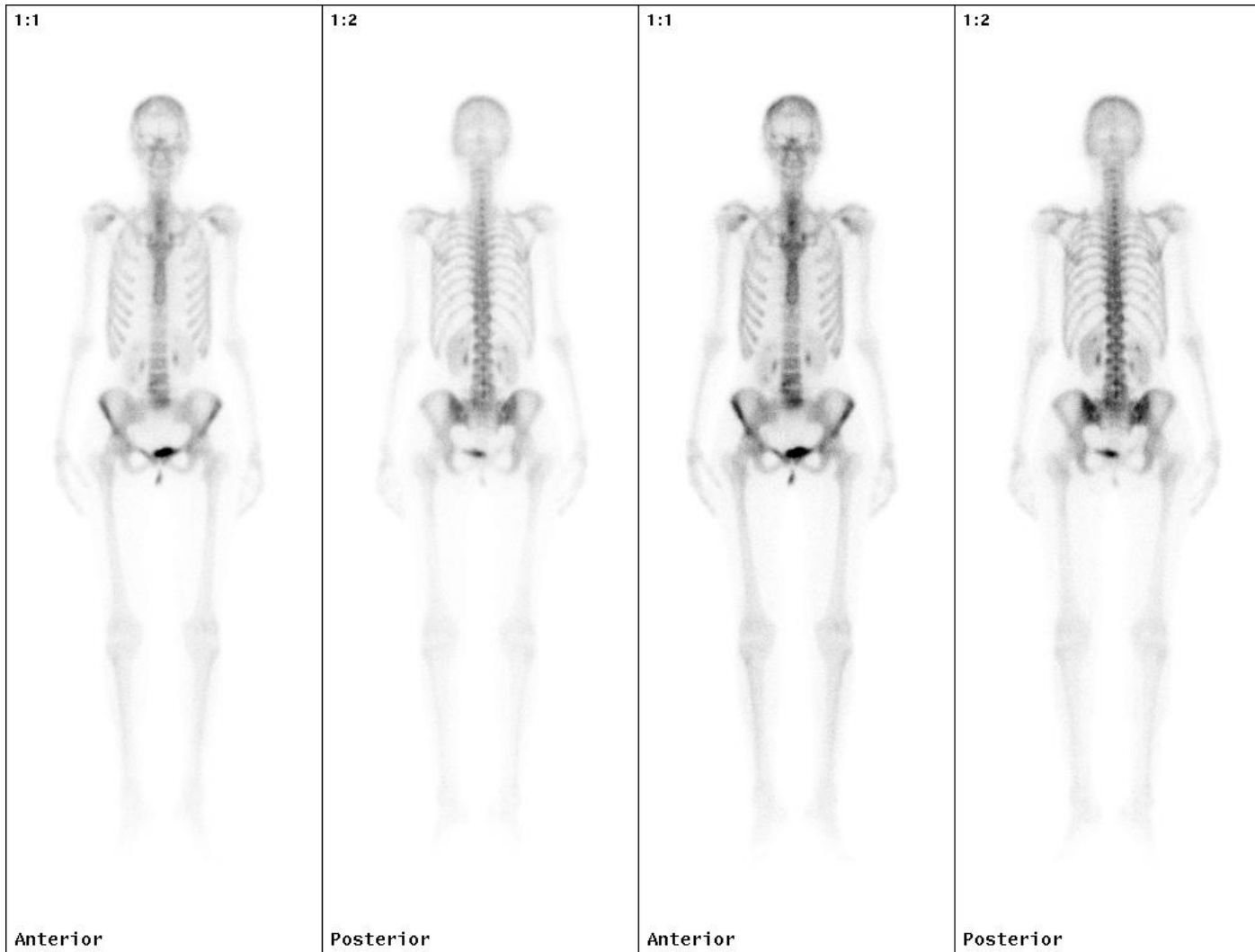
PATIENTNAME	PATIENTID	BIRTHDATE	GENDER	STUDYDESCRIPTION	SERIESDATE	SERIESTIME	MODALITY	SUBMODALITY	BODYPART	SERIESDESCRIPTION	SERIESFORMAT	PPSCOMMENTS
ANON01	ANON01	1953-01-01	M	Bone Scan	2014-01-01	13:00:00	NM	PRINT	Bone Scan	WB Tc-99m	GIF	
ANON02	ANON02	1953-01-01	F	Bone Scan	2014-01-01	13:00:00	NM	PRINT	Bone Scan	WB Tc-99m	GIF	
ANON03	ANON03	1942-01-01	M	Bone Scan	2013-01-01	13:00:00	NM	PRINT	Bone Scan	WB Tc-99m	GIF	
ANON04	ANON04	1962-01-01	M	Bone Scan	2014-01-01	13:00:00	NM	PRINT	Bone Scan	WB Tc-99m	GIF	
ANON05	ANON05	1942-01-01	M	Bone Scan	2014-01-01	13:00:00	NM	PRINT	Bone Scan	WB Tc-99m	GIF	
ANON06	ANON06	1942-01-01	M	Bone Scan	2013-01-01	13:00:00	NM	PRINT	Bone Scan	WB Tc-99m	GIF	
ANON07	ANON07	1959-01-01	M	Bone Scan	2013-01-01	13:00:00	NM	PRINT	Bone Scan	WB Tc-99m	GIF	
ANON08	ANON08	1942-01-01	M	Bone Scan	2013-01-01	13:00:00	NM	PRINT	Bone Scan	WB Tc-99m	GIF	
ANON09	ANON09	1941-01-01	M	Bone Scan	2014-01-01	13:00:00	NM	PRINT	Bone Scan	WB Tc-99m	GIF	
ANON10	ANON10	1953-01-01	F	Bone Scan	2014-01-01	13:00:00	NM	PRINT	Bone Scan	WB Tc-99m	GIF	
ANON11	ANON11	1953-01-01	M	Bone Scan	2014-01-01	13:00:00	NM	PRINT	Bone Scan	WB Tc-99m	GIF	
ANON112	ANON112	1967-01-01	F	Bone Scan	2014-01-01	13:00:00	NM	PRINT	Bone Scan	WB Tc-99m	GIF	
ANON117	ANON117	1967-01-01	F	Bone Scan	2014-01-01	13:00:00	NM	PRINT	Bone Scan	WB Tc-99m	GIF	
ANON12	ANON12	1962-01-01	M	Bone Scan	2014-01-01	13:00:00	NM	PRINT	Bone Scan	WB Tc-99m	GIF	
ANON13	ANON13	1949-01-01	F	Bone Scan	2014-01-01	13:00:00	NM	PRINT	Bone Scan	WB Tc-99m	GIF	
ANON134	ANON134	1945-01-01	M	Bone Scan	2014-01-01	13:00:00	NM	PRINT	Bone Scan	WB Tc-99m	GIF	
ANON135	ANON135	1929-01-01	M	Bone Scan	2014-01-01	13:00:00	NM	PRINT	Bone Scan	WB Tc-99m	GIF	
ANON137	ANON137	1945-01-01	F	Bone Scan	2014-01-01	13:00:00	NM	PRINT	Bone Scan	WB Tc-99m	GIF	
ANON138	ANON138	1945-01-01	M	Bone Scan	2014-01-01	13:00:00	NM	PRINT	Bone Scan	WB Tc-99m	GIF	
ANON14	ANON14	1962-01-01	M	Bone Scan	2014-01-01	13:00:00	NM	PRINT	Bone Scan	WB Tc-99m	GIF	
ANON141	ANON141	1945-01-01	F	Bone Scan	2014-01-01	13:00:00	NM	PRINT	Bone Scan	WB Tc-99m	GIF	
ANON142	ANON142	1929-01-01	M	Bone Scan	2014-01-01	13:00:00	NM	PRINT	Bone Scan	WB Tc-99m	GIF	
ANON15	ANON15	1941-01-01	M	Bone Scan	2014-01-01	13:00:00	NM	PRINT	Bone Scan	WB Tc-99m	GIF	
ANON16	ANON16	1949-01-01	F	Bone Scan	2014-01-01	13:00:00	NM	PRINT	Bone Scan	WB Tc-99m	GIF	
ANON17	ANON17	1945-01-01	M	Bone Scan	2013-01-01	13:00:00	NM	PRINT	Bone Scan	WB Tc-99m	GIF	
ANON18	ANON18	1947-01-01	M	Bone Scan	2014-01-01	13:00:00	NM	PRINT	Bone Scan	WB Tc-99m	GIF	
ANON19	ANON19	1945-01-01	M	Bone Scan	2013-01-01	13:00:00	NM	PRINT	Bone Scan	WB Tc-99m	GIF	
ANON20	ANON20	1949-01-01	F	Bone Scan	2014-01-01	13:00:00	NM	PRINT	Bone Scan	WB Tc-99m	GIF	
ANON21	ANON21	1939-01-01	M	Bone Scan	2014-01-01	13:00:00	NM	PRINT	Bone Scan	WB Tc-99m	GIF	
ANON22	ANON22	1942-01-01	M	Bone Scan	2014-01-01	13:00:00	NM	PRINT	Bone Scan	WB Tc-99m	GIF	
ANON23	ANON23	1941-01-01	M	Bone Scan	2014-01-01	13:00:00	NM	PRINT	Bone Scan	WB Tc-99m	GIF	
ANON24	ANON24	1947-01-01	M	Bone Scan	2014-01-01	13:00:00	NM	PRINT	Bone Scan	WB Tc-99m	GIF	
ANON25	ANON25	1945-01-01	M	Bone Scan	2013-01-01	13:00:00	NM	PRINT	Bone Scan	WB Tc-99m	GIF	
ANON26	ANON26	1950-01-01	M	Bone Scan	2013-01-01	13:00:00	NM	PRINT	Bone Scan	WB Tc-99m	GIF	
ANON27	ANON27	1939-01-01	M	Bone Scan	2013-01-01	13:00:00	NM	PRINT	Bone Scan	WB Tc-99m	GIF	
ANON28	ANON28	1930-01-01	M	Bone Scan	2013-01-01	13:00:00	NM	PRINT	Bone Scan	WB Tc-99m	GIF	
ANON29	ANON29	1933-01-01	M	Bone Scan	2013-01-01	13:00:00	NM	PRINT	Bone Scan	WB Tc-99m	GIF	
ANON30	ANON30	1942-01-01	M	Bone Scan	2013-01-01	13:00:00	NM	PRINT	Bone Scan	WB Tc-99m	GIF	
ANON31	ANON31	1944-01-01	M	Bone Scan	2013-01-01	13:00:00	NM	PRINT	Bone Scan	WB Tc-99m	GIF	
ANON32	ANON32	1947-01-01	M	Bone Scan	2013-01-01	13:00:00	NM	PRINT	Bone Scan	WB Tc-99m	GIF	
ANON33	ANON33	1944-01-01	M	Bone Scan	2013-01-01	13:00:00	NM	PRINT	Bone Scan	WB Tc-99m	GIF	
ANON34	ANON34	1942-01-01	M	Bone Scan	2014-01-01	13:00:00	NM	PRINT	Bone Scan	WB Tc-99m	GIF	

Applications@HERMES

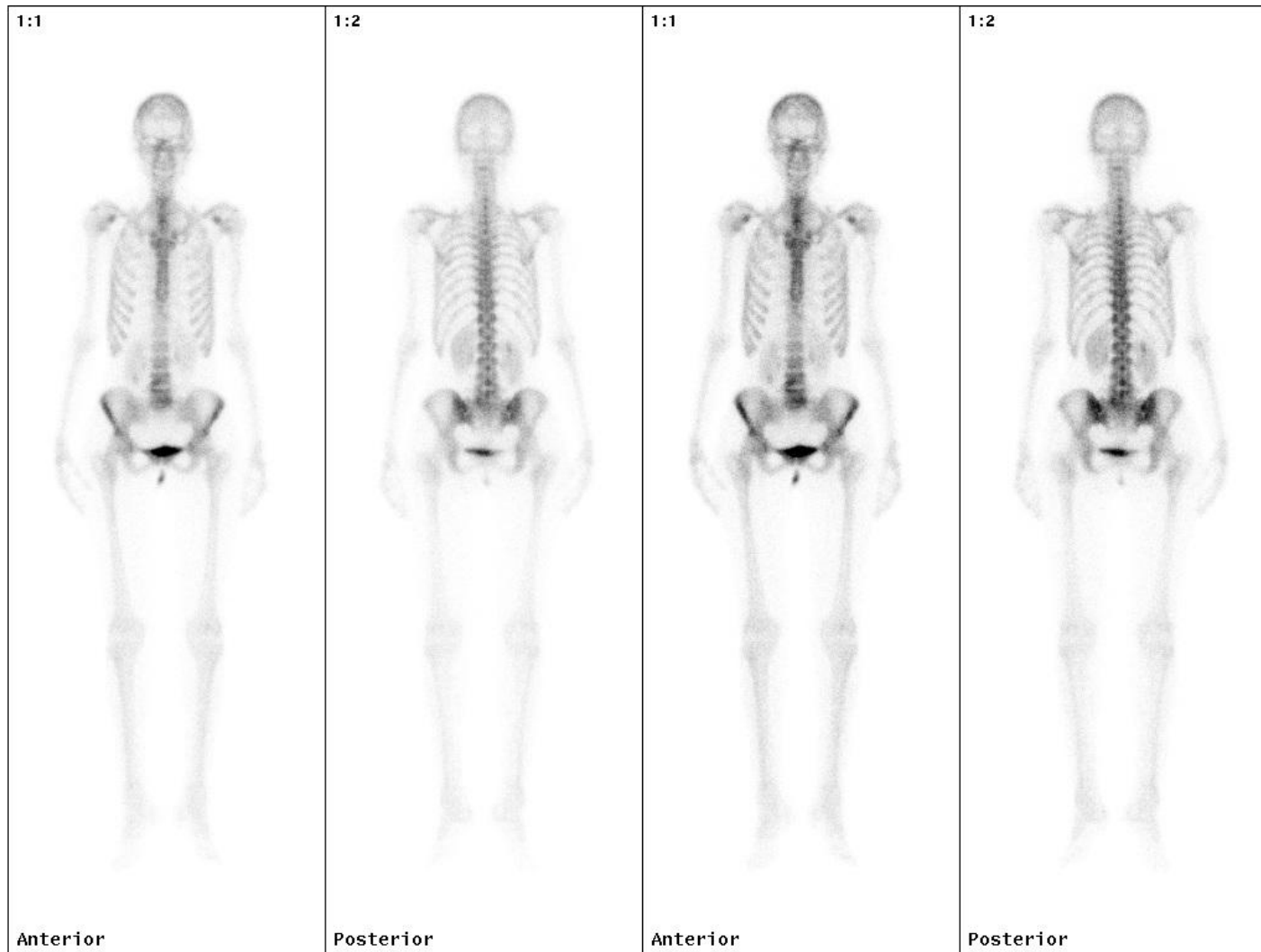
- Dynamic Study Display
- Kidney Analysis
- CINE Display
- Concatenate Images
- QGS & QPS Simultaneously
- Motion Correction
- DMSA Analysis (manuel)
- Show Multiple Prints
- Cardiac
  - QGS & QPS Simultaneously
- Oncology
  - Dynamic PET
- Miscellaneous
  - JADE Patient Viewer
  - Protocol Tool
  - Show Print/Movie
  - Copy to Images folder
  - Create/Edit TEXT
  - DICOM Export
  - Interfile Exporter
  - Start Application
  - Windows Printer

# Appendix III

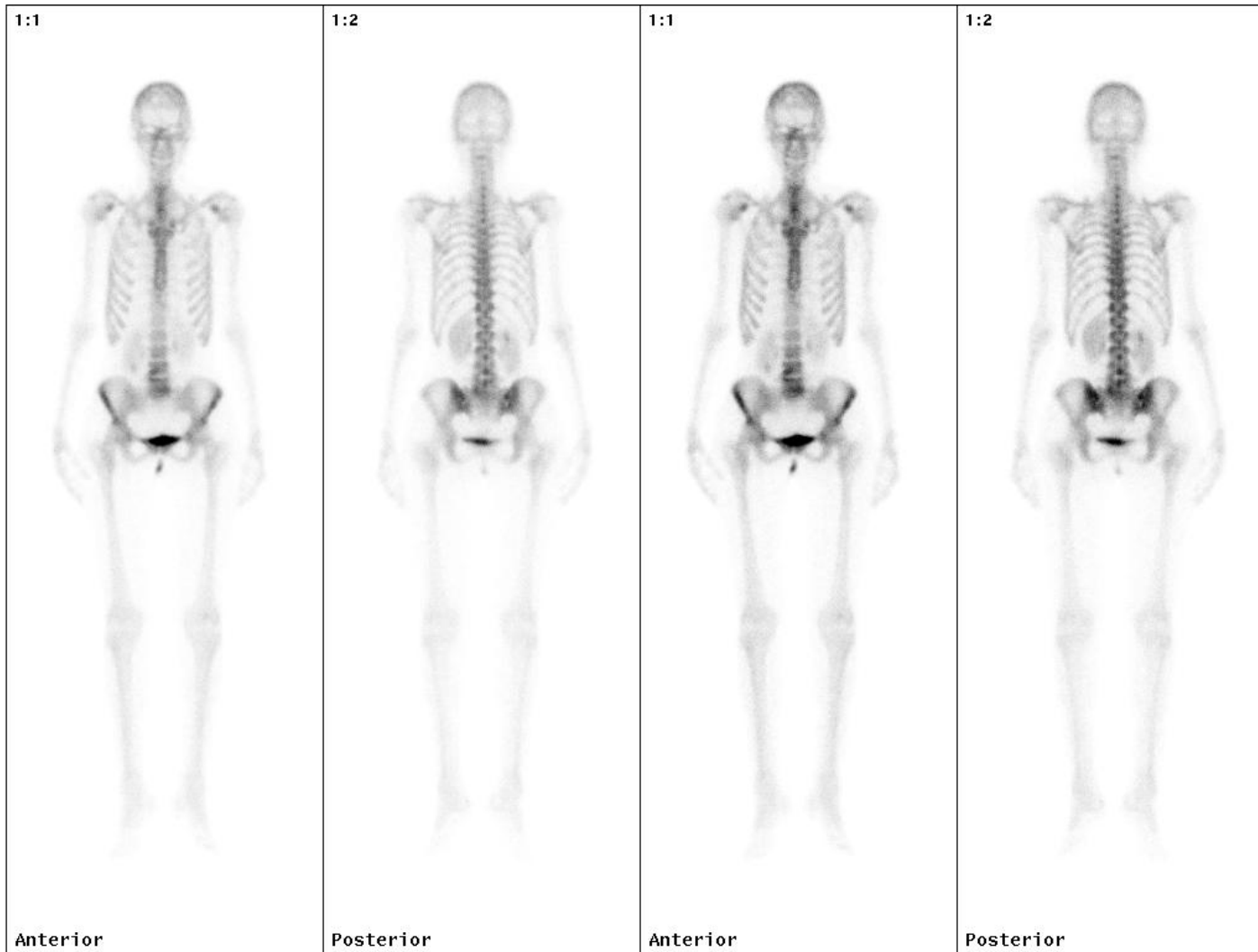
Full-count



Half-count



Pixon-processed





# Appendix IV

## Scoring Form

Radboudumc

Patient ID:

Physician ID:

Any visible lesion(s)?

- 1. Yes
- 2. No

Image Quality

- | Poor                  |                       | Medium                |                       | Good                  |
|-----------------------|-----------------------|-----------------------|-----------------------|-----------------------|
| 1                     | 2                     | 3                     | 4                     | 5                     |
| <input type="radio"/> | <input type="radio"/> | <input type="radio"/> | <input type="radio"/> | <input type="radio"/> |

Diagnostic Acceptability

- 1. Fully acceptable
- 2. Probably acceptable
- 3. Only acceptable under limited conditions
- 4. Unacceptable

Additional Comments:

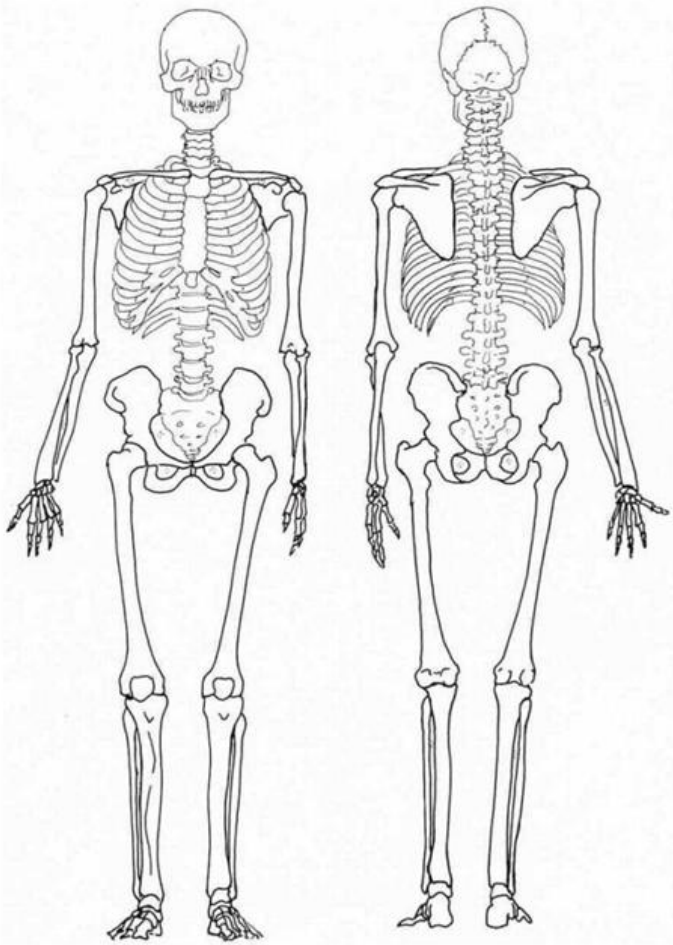
---

---

---

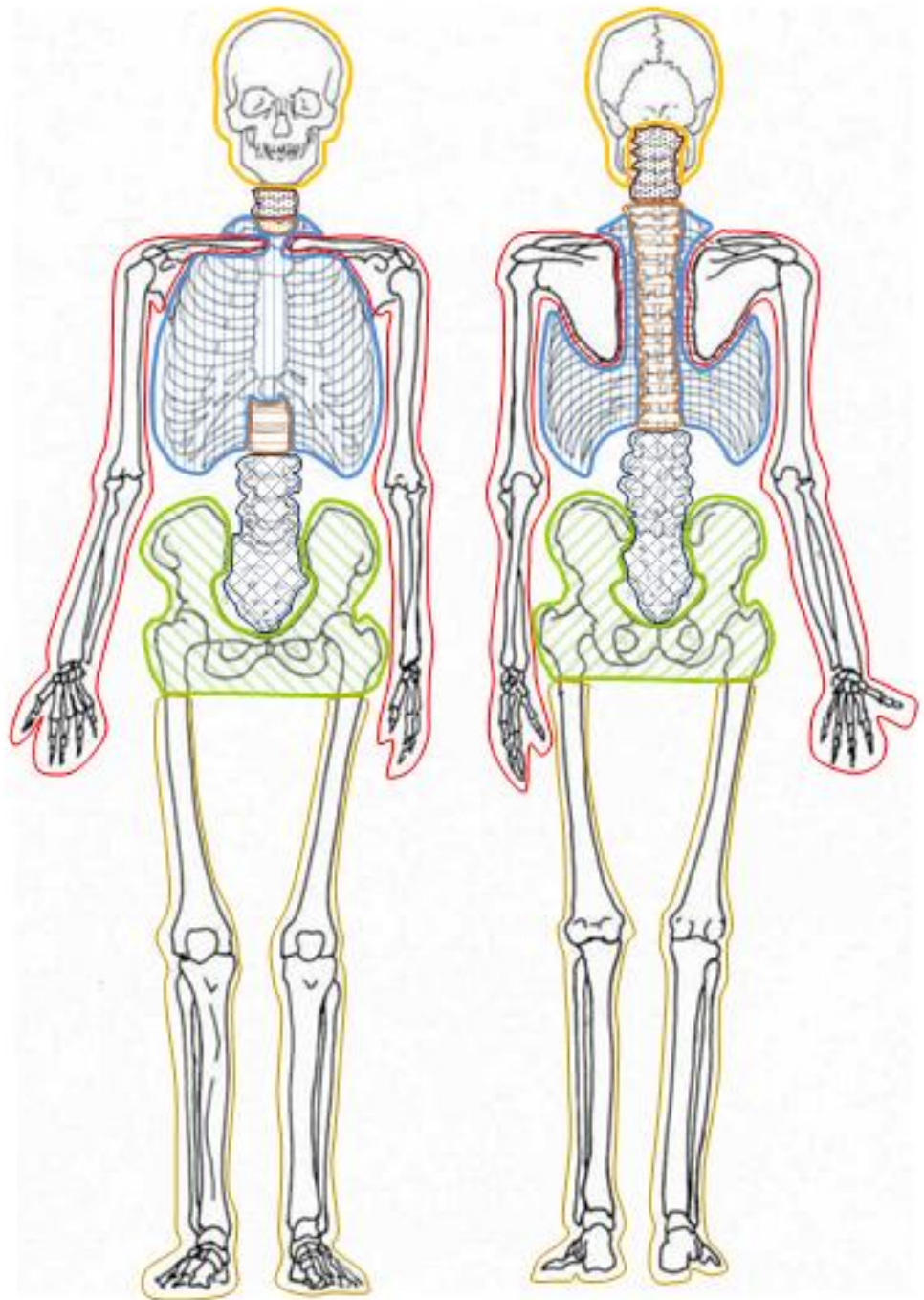
---

Lesion Location



# Appendix V

## Anatomical Regions



- Head
- Cervical Spine
- Chest
- Dorsal Spine
- Lumbosacral Spine
- Pelvis and Hips
- Upper Limb
- Lower Limb

### Instructions for the Scoring Form

#### Any visible lesion(s)?

Answer Yes/No if there are any visible lesions on the images.

#### Image Quality

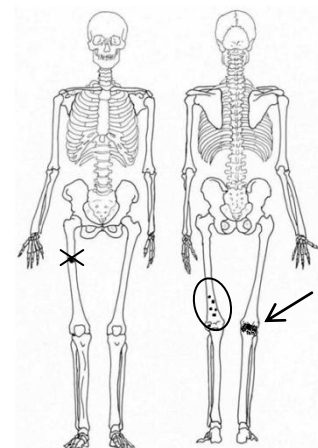
Score the image quality according to its general appearance (image resolution and noise levels) on a five-point numerical scale.

#### Diagnostic Acceptability

For diagnostic purposes, chose the best option for each presented image.

#### Lesion Location

- Consider the visualized lesions (if present);
- If they look like isolated metastatic lesions, mark the region with a cross;
- If they look like multiple and non-isolated metastatic lesions, mark those areas with a circle;
- If there is a lesion, but you are not certain about its metastatic origin, mark it with an arrow.



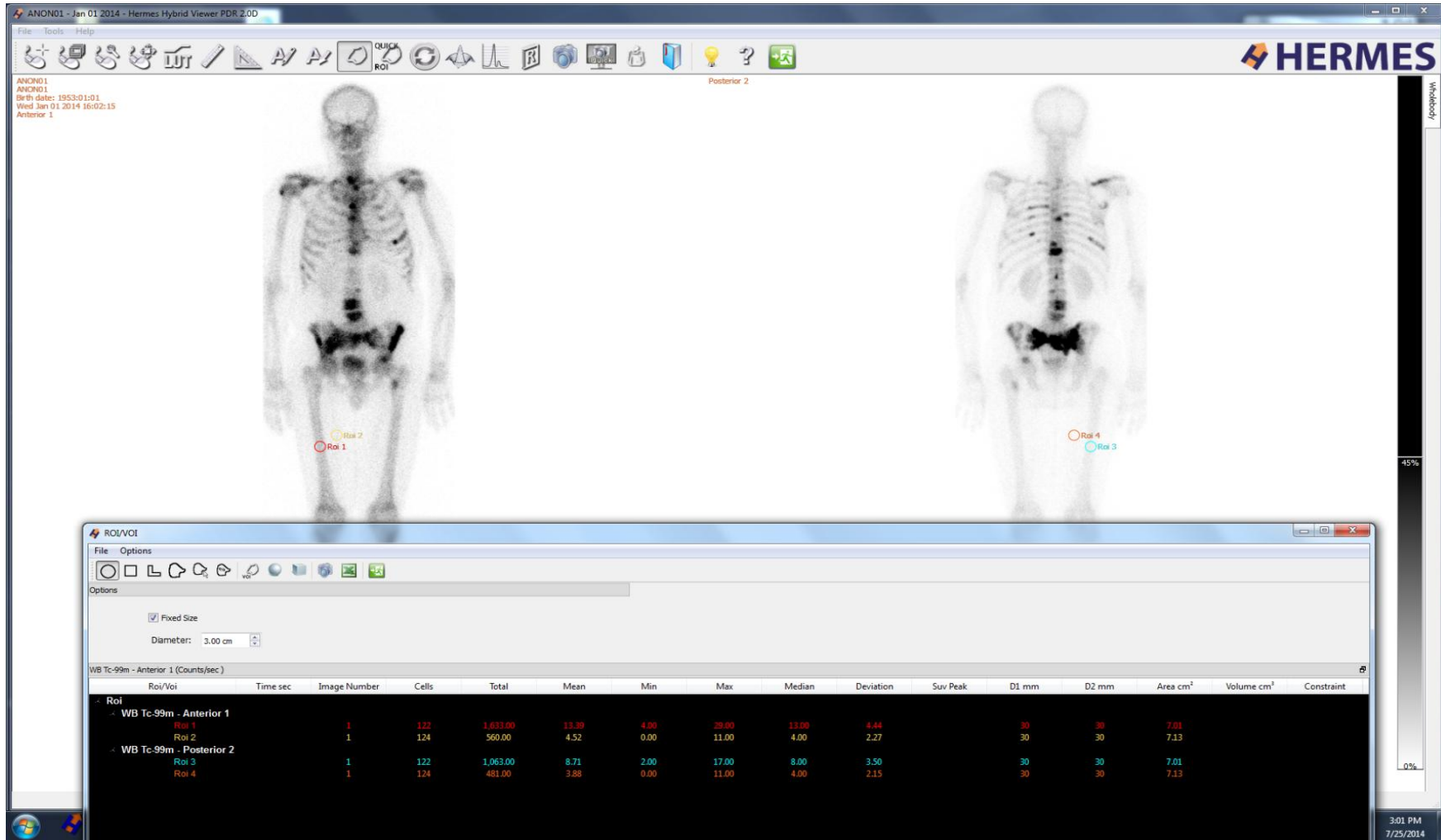
#### Additional Comments:

Please feel free to use this area to describe any points of interest, including the presence and location of non-metastatic (or even dubitative) lesions.

Thank you!

# Appendix VII

## Regions of Interest



***This page intentionally left blank***